Article

Developmental Cell

Formation of polarized contractile interfaces by self-organized Toll-8/Cirl GPCR asymmetry

Graphical abstract

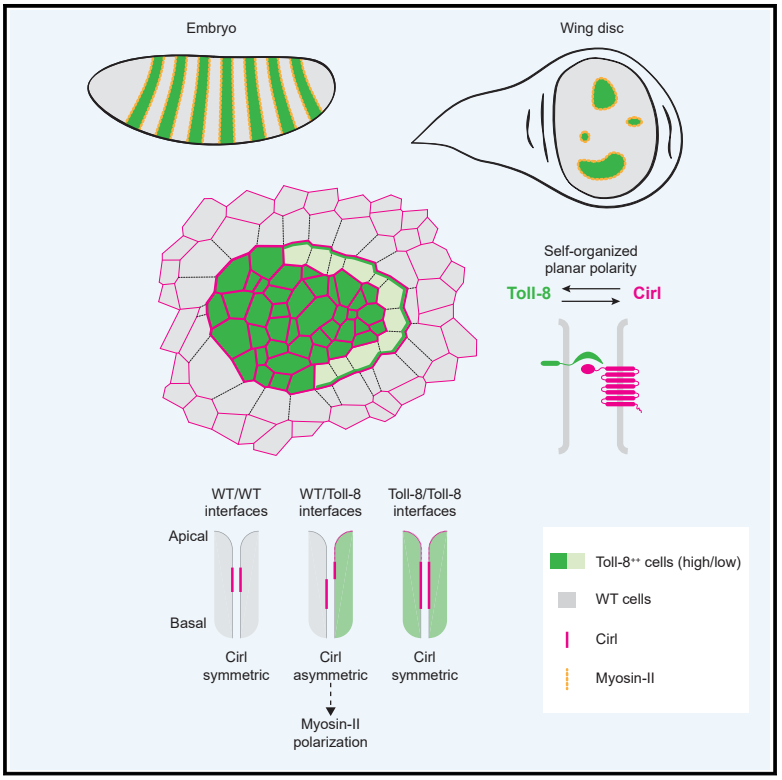

Highlights

- Asymmetric expression of a single Toll receptor leads to Myo-II polarization
- The adhesion GPCR Cirl binds to Toll-8 mediating Toll-8-induced Myo-II polarization
- Toll-8 boundaries generate a Cirl interfacial asymmetry that can polarize Myo-II
- Differences in Toll-8 levels lead to interdependent Toll-8 and Cirl planar polarity

Authors

Jules Lavalou, Qiyan Mao, Stefan Harmansa, ..., Stephane Audebert, Luc Camoin, Thomas Lecuit

Correspondence

qiyan.mao@univ-amu.fr (Q.M.), thomas.lecuit@univ-amu.fr (T.L.)

In brief

Lavalou, Mao et al. report that Toll-8 controls myosin-II planar polarity in *Drosophila* embryos and wing discs via a physical interaction with the GPCR Cirl/latrophilin. They show that Toll-8 expression boundaries generate a Cirl interfacial asymmetry and propose that it is a potential signal leading to myosin-II polarization.

Lavalou et al., 2021, Developmental Cell *56*, 1574–1588
June 7, 2021
https://doi.org/10.1016/j.devcel.2021.03.030

CellPress

CellPress
OPEN ACCESS

Developmental Cell

Article

Formation of polarized contractile interfaces by self-organized Toll-8/Cirl GPCR asymmetry

Jules Lavalou,[1,2,4] Qiyan Mao,[1,4,*] Stefan Harmansa,[1] Stephen Kerridge,[1] Annemarie C. Lellouch,[1] Jean-Marc Philippe,[1] Stephane Audebert,[3] Luc Camoin,[3] and Thomas Lecuit[1,2,5,*]

[1]Aix-Marseille Université & CNRS, IBDM - UMR7288 & Turing Centre for Living Systems, Marseille, France
[2]Collège de France, Paris, France
[3]Centre de Recherche en Cancérologie de Marseille, Marseille Proteomics, Aix-Marseille Université, Inserm, CNRS, Institut Paoli Calmettes, Marseille, France
[4]These authors contributed equally
[5]Lead contact
*Correspondence: qiyan.mao@univ-amu.fr (Q.M.), thomas.lecuit@univ-amu.fr (T.L.)
https://doi.org/10.1016/j.devcel.2021.03.030

SUMMARY

Interfaces between cells with distinct genetic identities elicit signals to organize local cell behaviors driving tissue morphogenesis. The *Drosophila* embryonic axis extension requires planar polarized enrichment of myosin-II powering oriented cell intercalations. Myosin-II levels are quantitatively controlled by GPCR signaling, whereas myosin-II polarity requires patterned expression of several Toll receptors. How Toll receptors polarize myosin-II and how this involves GPCRs remain unknown. Here, we report that differential expression of a single Toll receptor, Toll-8, polarizes myosin-II through binding to the adhesion GPCR Cirl/latrophilin. Asymmetric expression of Cirl is sufficient to enrich myosin-II, and Cirl localization is asymmetric at Toll-8 expression boundaries. Exploring the process dynamically, we reveal that Toll-8 and Cirl exhibit mutually dependent planar polarity in response to quantitative differences in Toll-8 expression between neighboring cells. Collectively, we propose that the cell surface protein complex Toll-8/Cirl self-organizes to generate local asymmetric interfaces essential for planar polarization of contractility.

INTRODUCTION

Dynamic cell behaviors that drive tissue morphogenesis are often organized at local cell interfaces. On one end, surface signaling between cells with distinct genetic identities, via compartmentalized expression of ligands and receptors, can generate mechanical barriers in developmental (Dahmann et al., 2011) or pathological contexts (Bielmeier et al., 2016). For instance, expression boundaries of Eph-Ephrin or Leucine-rich repeat (LRR) proteins prevent cell mixing in vertebrate and invertebrate models (Dahmann et al., 2011; Fagotto et al., 2013; Karaulanov et al., 2006; Milán et al., 2001; Paré et al., 2019; Smith and Tickle, 2006; Tomás et al., 2011). On the other end, surface signaling can also orient fluid mechanical interfaces in the context of tissue planar polarity. Surface proteins in the core planar cell polarity (PCP) pathway, such as Flamingo/CELSR and Frizzled, translate tissue-scale cues into vectorial cell polarity known to control planar polarized actomyosin contractility (Aw and Devenport, 2017; Nishimura et al., 2012). Tissue-level gradients of the Fat/Dachsous adhesion molecules in the Fat-PCP pathway induce planar polarized accumulation of the myosin Dachs at cell interfaces to drive dynamic cell rearrangements (Bosveld et al., 2012).

The early *Drosophila* embryo is an excellent system to investigate how cell groups with distinct genetic identities generate planar polarized mechanical interfaces. In the ventrolateral ectoderm, myosin-II (Myo-II) is enriched at vertical interfaces between anteroposterior (AP) neighbors, which produces polarized actomyosin contractility powering AP axis extension (Bertet et al., 2004; Blankenship et al., 2006; Irvine and Wieschaus, 1994; Zallen and Wieschaus, 2004). The amplitude and polarity of actomyosin contractility appear to be controlled by diverse cell surface proteins. Levels of Myo-II activation at cell interfaces are quantitatively controlled by G protein-coupled receptor (GPCR) signaling (Garcia De Las Bayonas et al., 2019; Kerridge et al., 2016), whereas the polarized enrichment of Myo-II between AP neighbors appears to be governed by several Toll receptors, Toll-2,6,8 (Paré et al., 2014). Interactions between pair-rule genes define periodic and partially overlapping stripes of Toll receptors perpendicular to the AP axis (Paré et al., 2014). Thus, each column of cells expresses a different combination of Toll-2,6,8, which are thought to be collectively required for planar polarized Myo-II activity (Paré et al., 2014; Tetley et al., 2016). Toll receptors belong to the LRR super family and are well known for their functions in developmental patterning and innate

immunity (Anthoney et al., 2018). They recently emerged as conserved molecules involved in embryonic axis elongation in different arthropod species (Benton et al., 2016; Paré et al., 2014). How Toll receptors define polarized mechanical interfaces, and whether they interact with other cell surface receptors such as GPCRs, remain largely unexplored.

Here, we investigated how Toll receptors control Myo-II planar polarity in conjugation with GPCR signaling in the *Drosophila* embryonic ectoderm and larval wing disc epithelium. In contrast to the combinatorial Toll code model, we show that a single Toll receptor, Toll-8, enriches Myo-II at its expression boundary. This enrichment does not require the cytoplasmic tail of Toll-8. Further, we identified a Toll-8-binding partner, the adhesion GPCR Cirl/latrophilin, which is required for Toll-8-mediated Myo-II enrichment in both embryos and wing discs. We show in wing discs that Cirl asymmetry is sufficient to enrich Myo-II, and we observed an interfacial asymmetry in Cirl apicobasal localization at Toll-8 expression boundaries. Moreover, when neighboring cells express different levels of Toll-8 in wing discs, both Toll-8 and Cirl exhibit robust and mutually dependent planar polarity. Our study thus reveals that Toll-8 and Cirl form a cell surface protein complex essential for planar polarized actomyosin activity, generate local asymmetric interfaces, and co-polarize in a self-organized manner.

RESULTS

Asymmetric expression of a single Toll receptor leads to Myo-II polarization in embryos

In the *Drosophila* embryonic ectoderm, it has been hypothesized that *trans*-interactions between different Toll receptors across cell-cell interfaces signal to polarize junctional Myo-II (Paré et al., 2014). In light of the observation that ectopic expression of Toll-2 or Toll-8 alone induces Myo-II enrichment late in embryogenesis (Paré et al., 2014), we first tested the simplest hypothesis that a single Toll is sufficient to polarize junctional Myo-II in the embryonic ectoderm. To this end, we injected embryos with double-stranded RNAs (dsRNAs) targeting Toll-2,6,7 (*toll-2,6,7* RNAi), leaving only endogenous Toll-8 expressed in vertical stripes (Figure S1A), and observed Myo-II with mCherry-tagged Myo-II regulatory light chain (MRLC-Ch). We found Myo-II specifically enriched at the interfaces between Toll-8 expressing and non-expressing cells (Figures S1A–S1D), suggesting that asymmetric expression of a single Toll, Toll-8, leads to Myo-II enrichment independent of other Toll receptors.

To assess the sufficiency of Toll-8 asymmetry in Myo-II polarization independent of the anteroposterior (AP) patterning system, we engineered embryos expressing a single stripe of Toll-8 along the AP axis that runs orthogonal to the endogenous Toll-2,6,8 stripes, using an *intermediate neuroblasts defective* (*ind*) enhancer (Stathopoulos and Levine, 2005) (*ind-Toll-8-HA*, Figure 1A). We monitored Myo-II with GFP-tagged Myo-II regulatory light chain (MRLC-GFP) and detected a Myo-II-enriched cable at the ventral boundary between ectopic Toll-8 expressing and wild-type cells (Figures 1A and 1B, Toll-8^{FL}). Note that this ectopic Myo-II cable runs along the AP axis and perpendicular to the endogenous Myo-II planar polarity. By contrast, no Myo-II enrichment is detected at homotypic Toll-8 interfaces within the ind-Toll-8 domain (Figure 1C). Myo-II enrichment at the ventral border of ind-Toll-8 is comparable with that at the endogenous boundaries of the Toll-8 expression domain (Figure S1E). When we deleted the LRRs from the Toll-8 extracellular domain, Toll-8 was no longer localized to the plasma membrane and failed to accumulate Myo-II (Figures 1A, 1B, and 1D, Toll-$8^{\Delta LRR}$). Consistent with an upregulation of cortical tension, the boundary of Toll-8-expressing cells was smoother when full-length Toll-8 (Toll-8^{FL}) was expressed compared with Toll-$8^{\Delta LRR}$ (Figures 1B and 1E; smoothness defined by the ratio of distance between terminal vertices over total junctional length).

When we injected *ind-Toll-8-HA* embryos with dsRNAs targeting only endogenous Toll-2,6,8 (*toll-2,6,8* RNAi), Myo-II was still enriched at the boundary of ectopic Toll-8-expressing cells (Figures 1F, 1G, and S1F). This boundary was also smooth (Figures 1F, 1H, and S1F). Altogether, we conclude that an interface defined by asymmetric expression of a single Toll, Toll-8, is sufficient to polarize Myo-II.

Asymmetric expression of a single Toll receptor polarizes Myo-II in wing discs

To further dissect the capacity of Toll-8 to elicit junctional Myo-II enrichment, we used clonal analysis to generate random interfaces between wild-type and Toll-8-overexpressing cells in larval wing imaginal discs since clonal analysis is not possible in early embryos. Wing imaginal discs exhibit polarized supracellular cables of Myo-II at the periphery of the pouch region near the hinge (LeGoff et al., 2013). Toll receptor overexpression causes wing developmental defects (Yagi et al., 2010), and Toll-8 is expressed in the wing hinge region but absent in most of the pouch region (Alpar et al., 2018; Yagi et al., 2010). We induced clones overexpressing Toll-8-GFP in the larval wing disc epithelium and monitored Myo-II localization with MRLC-Ch 24 h after clone induction in the wing pouch (Figure 2A). This resulted in striking junctional Myo-II enrichment specifically at the boundary of Toll-8 overexpressing clones, in contrast to homotypic interfaces within the Toll-8 clone (Figures 2A–2C). As in embryos, we found that in the absence of the LRRs, Toll-8 was no longer localized to the plasma membrane and failed to polarize Myo-II (Figures 2D and 2E, Toll-$8^{\Delta LRR}$). Toll-8^{FL} clones were more compact with a smoother boundary compared with Toll-$8^{\Delta LRR}$ clones (Figures 2D and 2F; smoothness defined by the mean angle between neighboring vertices, Figure 2A).

The cytoplasmic domain of Toll proteins is necessary for canonical Toll signal transduction (Anthoney et al., 2018). To test whether the cytoplasmic domain of Toll-8 is required for Myo-II enrichment, we generated wing disc clones overexpressing a truncated version of Toll-8, removing its cytoplasmic domain (Toll-$8^{\Delta Cyto}$). Surprisingly, Myo-II was still enriched at the boundary of Toll-$8^{\Delta Cyto}$-overexpressing clones (Figures 2D and 2E), and the clonal boundary was still smooth compared with Toll-$8^{\Delta LRR}$ clones (Figures 2D and 2F). We conclude that the cytoplasmic domain of Toll-8 is dispensable for Myo-II polarization. We observed similar results for Toll-6 and Toll-2 (Figures S2A and S2B). This indicates that the signaling events leading to Myo-II enrichment at the boundary between Toll-8-expressing and non-expressing cells may require another protein, presumably interacting with Toll-8 at the cell surface.

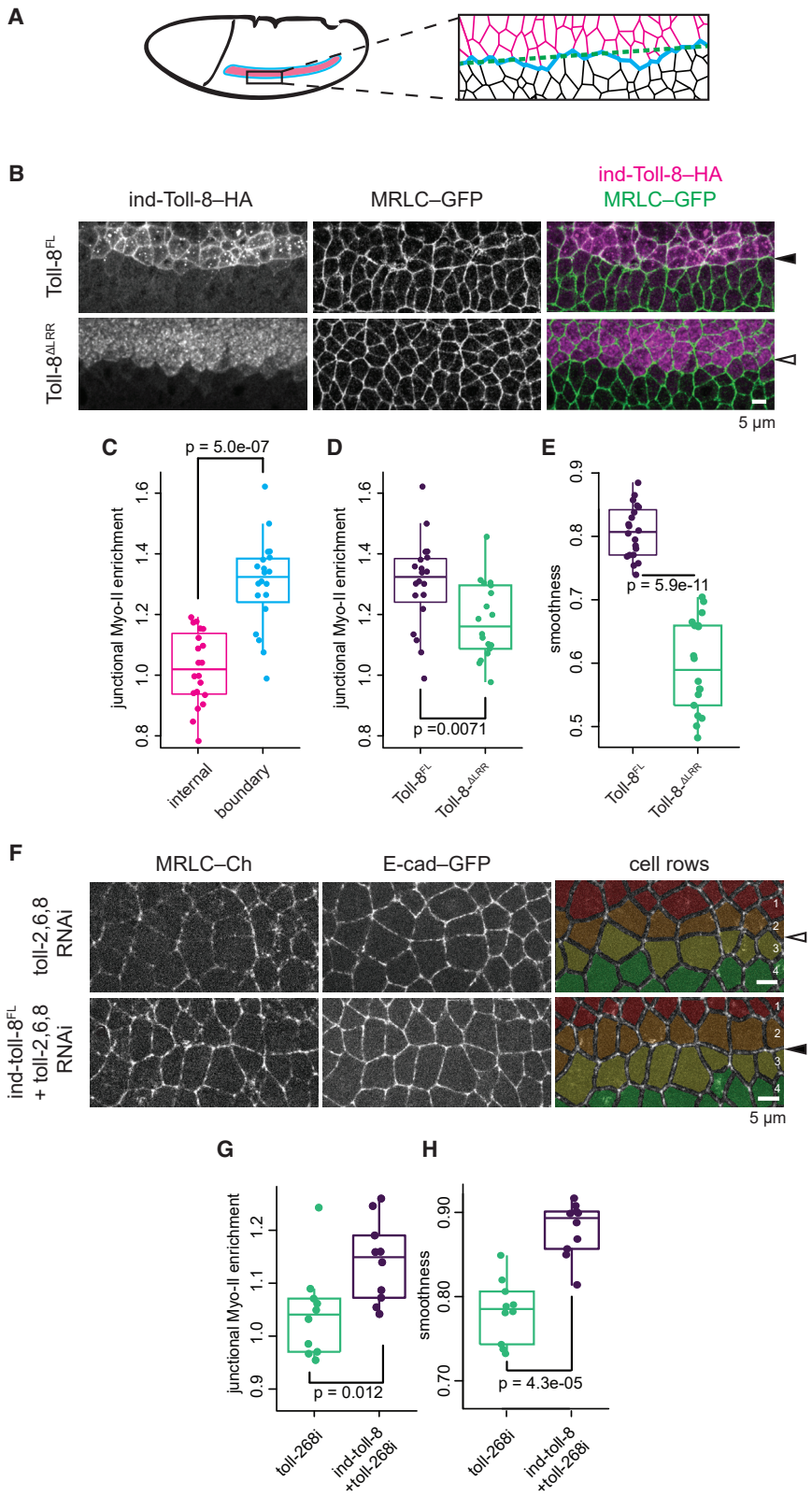

Figure 1. Toll-8 asymmetry leads to Myo-II enrichment in embryos, independent of other Toll receptors

(A) Schema of an embryo expressing ind-Toll-8-HA and cell interfaces around the ventral boundary of ind-Toll-8–HA. Pink, black and blue denote interfaces within the ind-Toll-8-HA stripe, the wild-type tissue, and at the ventral boundary of the ind-Toll-8-HA, respectively. Dashed line in green: distance between the first and last vertices of the ind-Toll-8-HA ventral boundary.

(B) Anti-Toll-8-HA and anti-MRLC-GFP signals in *Drosophila* stage-7 embryos expressing full-length Toll-8 (Toll-8^{FL}, top, n = 20) or Toll-8 with the extracellular LRRs removed (Toll-$8^{\Delta LRR}$, bottom, n = 18) driven by the *ind* promoter. Myo-II is enriched at the ventral boundary of the ind-Toll-8^{FL}-HA stripe (filled arrowhead) but not for ind-Toll-$8^{\Delta LRR}$-HA (empty arrowhead).

(C) Junctional Myo-II enrichment relative to wild-type tissue within the ind-Toll-8^{FL}-HA stripe (pink) or at the ventral boundary of the ind-Toll-8^{FL}-HA stripe (blue) for the condition shown in (B, top).

(D and E) Junctional Myo-II enrichment (D) and boundary smoothness (E) at the ventral *ind* boundary for the conditions shown in (B).

(F) Stills from time-lapse movies in *wt* embryos (top, n = 10) or embryos expressing ind-Toll-8^{FL}-HA injected with dsRNAs against Toll-2,6,8 (bottom, n = 10). Pseudo colors mark 4 cell rows. In the absence of endogenous Toll-2,6,8, Myo-II is still enriched at the *ind* ventral boundary (filled arrowhead).

(G and H) Junctional Myo-II enrichment (G) and boundary smoothness (H) at the ventral *ind* boundary for the conditions shown in (F).

CellPress
OPEN ACCESS

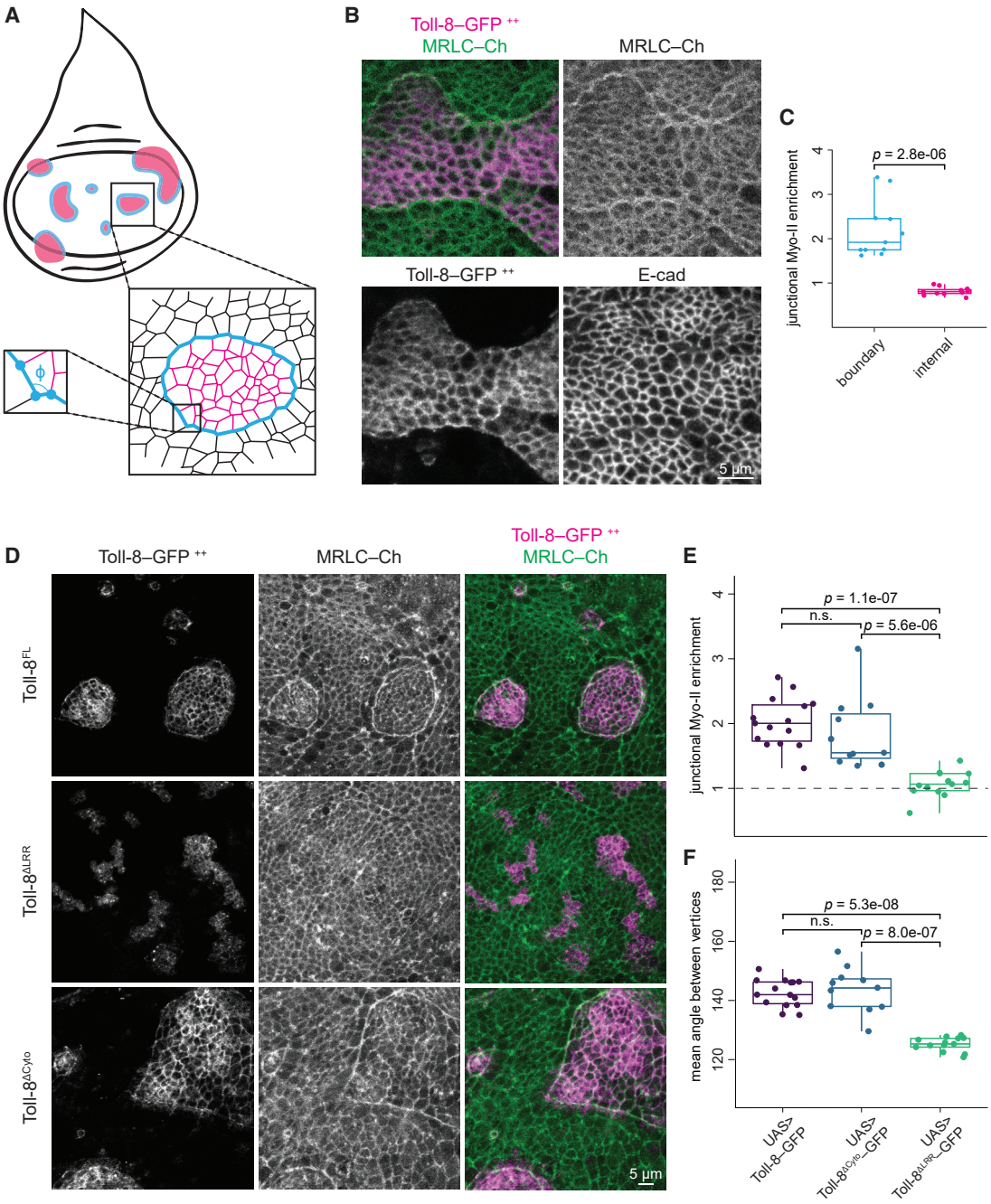

Figure 2. Toll-8 asymmetry leads to Myo-II enrichment in wing discs, independent of the Toll-8 cytoplasmic tail

(A) Schema showing wing disc clones and cell interfaces around a clone. Pink, black, and blue denote interfaces within the clone, within the wild-type tissue, and at the clonal boundary, respectively. φ is the angle between neighboring vertices at the clonal boundary.

(B) Fixed Toll-8-GFP, MRLC-Ch, and E-cadherin signals from wing disc clones overexpressing full-length Toll-8 (n = 11). Myo-II is enriched at the clone boundary but not inside the clone.

(C) Junctional Myo-II enrichment relative to wild-type tissue within (pink) or at the boundary of (blue) Toll-8 overexpressing clones for the condition shown in (B).

(D) Fixed Toll-8-GFP and MRLC-Ch signals from wing disc clones overexpressing full-length Toll-8 (Toll-8^{FL}, top, n = 15), Toll-8 with the extracellular LRRs removed (Toll-$8^{\Delta LRR}$, middle, n = 11), or Toll-8 with the intracellular cytoplasmic tail removed (Toll-$8^{\Delta Cyto}$, bottom, n = 13). Myo-II enrichment does not require the cytoplasmic tail of Toll-8.

(E and F) Junctional Myo-II enrichment (E) and boundary smoothness (F) at clone boundaries for the conditions shown in (D).

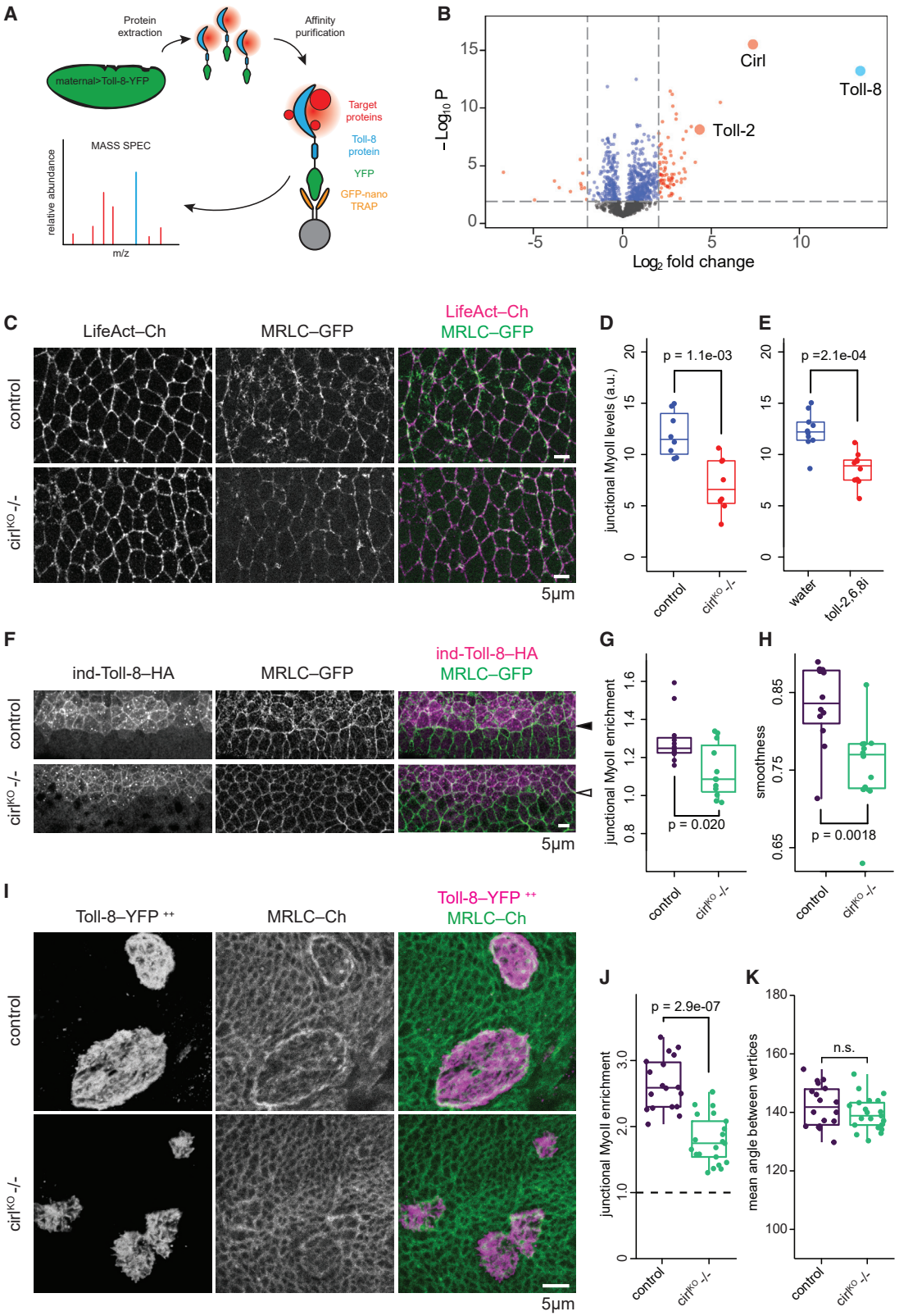

Figure 3. The aGPCR Cirl interacts physically with Toll-8 and is necessary for Myo-II enrichment induced by Toll-8.

(A) Affinity purification-mass spectrometry using embryos overexpressing the Toll-8-YFP fusion protein (Toll-8 in blue, YFP in green, potential binding targets in red) and the GFP-Trap (nanobody against GFP/YFP in orange, agarose bead in gray).

(legend continued on next page)

Cirl/latrophilin binds to Toll-8 and mediates Toll-8-induced Myo-II enrichment

To look for binding partners of Toll-8, we performed affinity purification-mass spectrometry experiments using lysates isolated from embryos overexpressing Toll-8-YFP as a bait (Figure 3A and STAR methods). Of the specifically bound proteins that interact directly or indirectly in a complex with Toll-8, Cirl was the most abundant target (Figure 3B; Table S1) and of particular interest since it is a GPCR. Cirl is the *Drosophila* homolog of vertebrate latrophilin, a member of the adhesion GPCR (aGPCR) subfamily (Scholz et al., 2015; Schöneberg and Prömel, 2019). Interestingly, the Toll-8 extracellular domain shares sequence similarities with that of the human LRR protein FLRTs (Dolan et al., 2007), which are known to form protein complexes with human latrophilins (Boucard et al., 2014; Li et al., 2020; O'Sullivan et al., 2012; Sando et al., 2019; del Toro et al., 2020). We also recovered Toll-2 as a significant Toll-8-binding partner *in vivo* (Figure 3B; Table S1), in agreement with previous findings *in vitro* (Paré et al., 2014).

Using a Cirl-RFP knockin line (Scholz et al., 2017) to visualize endogenous Cirl, we found that Cirl localized to the membrane and was enriched at cell-cell interfaces around adherens junctions in both the embryo and the wing disc (Figures S3A and S3B). We next asked whether Cirl is required for Myo-II enrichment in the embryo. *cirl* maternal and zygotic mutant embryos showed delayed extension of the embryonic axis (Figures S3C and S3D), reduced cell intercalation (Figures S3E and S3F; Video S1), and a strong reduction of junctional Myo-II in the ectoderm (Figures 3C and 3D), resembling Myo-II reduction observed in *toll-2,6,8* RNAi embryos (Figures 3E and S1A). Thus, *cirl* is required for junctional Myo-II enrichment in the embryo. We observed that Myo-II is reduced at vertical junctions both in *toll-2,6,8* RNAi embryos and in *cirl* mutant embryos (Figures S3G and S3H). However, all junctions show lower Myo-II levels in *cirl* mutant embryos (Figure S3H). Myo-II planar polarity tends to be reduced in both conditions but is significantly reduced only in *toll-2,6,8* RNAi embryos (Figure S3I). We suggest that in the absence of Cirl, Toll receptors can still polarize Myo-II via other GPCRs than Cirl.

We further tested whether Cirl is required for Toll-8-induced polarization of Myo-II by comparing the ventral boundary of *ind-Toll-8-HA* stripe in wild-type and *cirl*-null mutant embryos. In the absence of Cirl, we found a strong reduction in Myo-II enrichment at the boundary of Toll-8 stripe, which was also less smooth (Figures 3F–3H). Moreover, in *cirl*-null mutant wing discs, we observed a similar reduction in Myo-II enrichment at the boundary of Toll-8 clones (Figures 3I and 3J). Note that Myo-II enrichment was not completely abolished, and the clonal boundary was still smooth (Figure 3K), suggesting that other molecules in addition to Cirl may interact with Toll-8 to confer Myo-II enrichment at clone boundaries in the wing disc. Taken together, we conclude that Toll-8 and Cirl physically and functionally interact to polarize Myo-II at interfaces between Toll-8-expressing and non-expressing cells.

Cirl asymmetric interfaces lead to Myo-II enrichment

Interestingly, we observed that Myo-II was enriched on both sides of the interface between Toll-8 expressing and non-expressing cells (Figures S4A and S4A′), indicating that Myo-II is also enriched in cells that do not express Toll-8. We thus tested whether Cirl mediates Myo-II enrichment on both sides of the interface. To this end, we performed mosaic analysis with a repressible cell marker (MARCM) in wing discs and induced *cirl*-null mutant clones either adjacent to (Figure 4A) or coincident with (Figure 4B) Toll-8-overexpressing clones. We expected that removing Cirl from one side should lead to a reduction in Myo-II enrichment at the clone boundary due to a loss of Myo-II enrichment in cells where Cirl is absent. Surprisingly, when Cirl was only absent from neighboring cells, Myo-II was enriched at the Toll-8 boundary at similar levels to control interfaces (Figure 4A, compare orange and cyan arrows, quantified in Figure 4C) and on both sides of the clone boundary (Figure S4B). Similarly, when Cirl was only absent from cells overexpressing Toll-8, Myo-II was still enriched at similar levels at the clone boundary (Figure 4B, quantified in Figure 4C) and on both sides of the clone boundary (Figure S4C). Thus, Cirl is dispensable in either Toll-8-expressing or -responding/contacting cells. This is remarkable since Cirl must be present on at least one side of Toll-8-overexpressing clones, as the complete removal of Cirl on both sides significantly reduces Myo-II enrichment (Figure 3J). We thus hypothesized that (1) the role of Toll-8 is to induce an asymmetry of Cirl activity at the clonal boundary and that (2) Cirl asymmetric interfaces enrich Myo-II. To test the latter, we generated *cirl* mutant clones in the wing disc without overexpressing Toll-8. We reasoned that at the *cirl* mutant clonal interface Cirl localization and activity is *de facto* asymmetric. This is supported by the observation that Cirl is still localized in wild-type cell interfaces in contact with *cirl* mutant cells (Figure S4D, yellow arrowhead). We found that Myo-II was indeed enriched at the boundary of *cirl* mutant clones and that the boundary was smooth compared with control clones (Figures 4D–4F). This is similar to Toll-8-overexpressing clones, albeit to a lesser extent. We thus conclude

(B) Volcano plot showing differential levels (x axis) and p values (y axis) of proteins identified by mass spectrometry in embryos overexpressing Toll-8-YFP versus *wt* embryos. Vertical dashed lines denote the cutoff for $\log_2$|Fold Change| as 2. Horizontal dashed line denotes the cutoff for p value as 0.01. Toll-8 (bait), Cirl, and Toll-2 are highlighted.

(C) Stills from time-lapse movies in *wt* (top, n = 8) or $cirl^{KO}$ −/− (bottom, n = 8) embryos. LifeAct-Ch marks cell outlines. Junctional Myo-II is reduced in $cirl^{KO}$ −/− null mutant embryos.

(D) Mean junctional Myo-II levels for the conditions shown in (C).

(E) Mean junctional Myo-II levels in embryos injected with water (n = 10) or dsRNAs against Toll-2,6,8 (n = 10) (related to Figures S1A and S1B).

(F) Anti-Toll-8-HA and anti-MRLC-GFP signals in *wt* (top, n = 12) or $cirl^{KO}$ −/− (bottom, n = 12) embryos expressing full-length Toll-8 under the *ind* promoter. Myo-II is reduced at the *ind* ventral boundary in $cirl^{KO}$ −/− embryos (empty arrowhead).

(G and H) Junctional Myo-II enrichment (G) and boundary smoothness (H) at the ventral *ind* boundary for the conditions shown in (F).

(I) Fixed Toll-8-YFP and MRLC-Ch signals from wing disc clones overexpressing full length Toll-8 in *wt* (top, n = 18) or $cirl^{KO}$ −/− (bottom, n = 21) wing discs. Myo-II is reduced at the boundary of Toll-8 overexpressing clones in $cirl^{KO}$ −/− wing discs.

(J and K) Junctional Myo-II enrichment (J) and boundary smoothness (K) at clone boundaries for the conditions shown in (I).

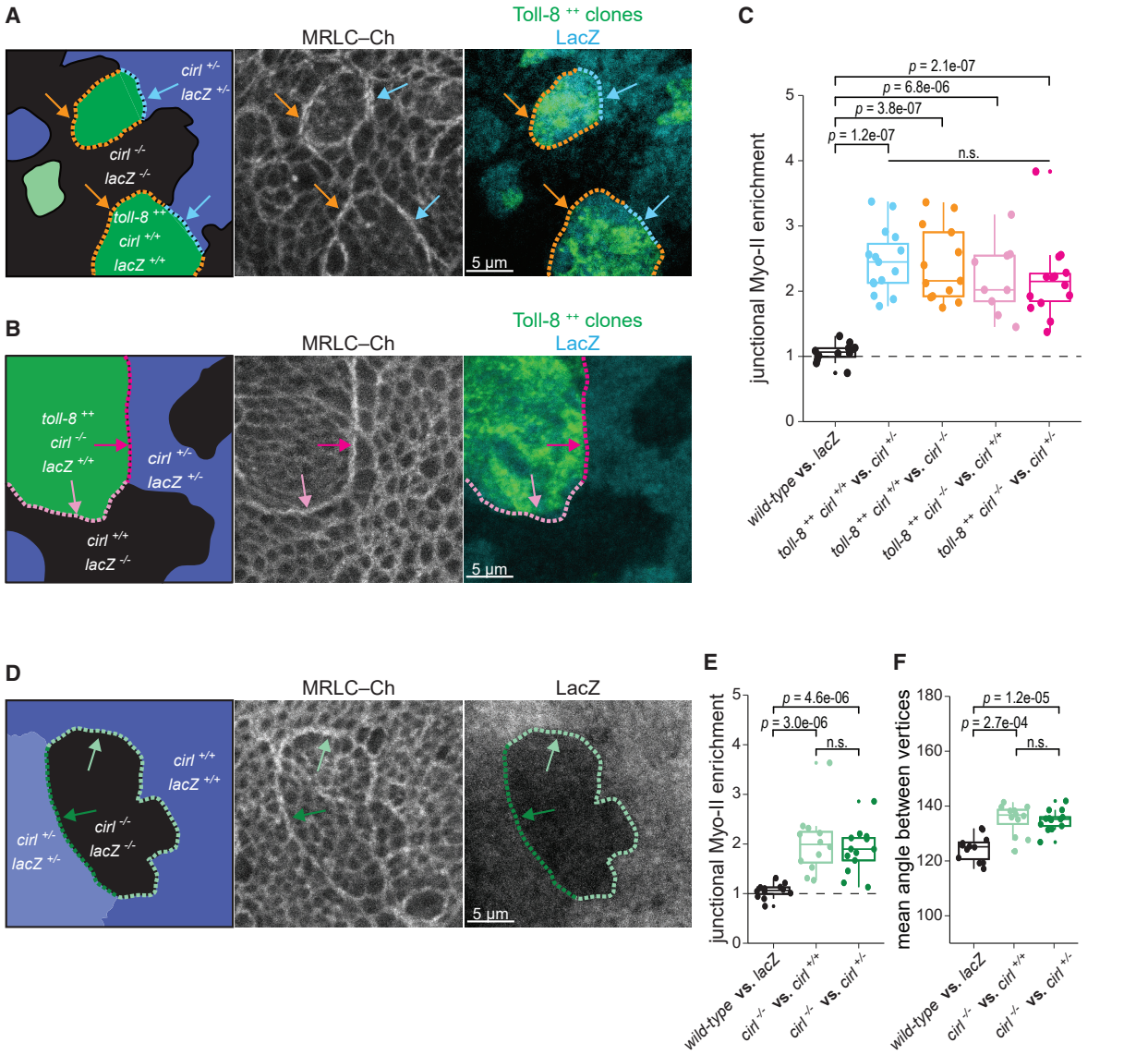

Figure 4. Cirl asymmetric expression leads to Myo-II enrichment

(A) MARCM clones in a wing disc where clones overexpressing Toll-8-YFP (*toll-8*$^{++}$ in green) are juxtaposed to control cells heterozygous (*cirl*$^{+/-}$ in blue, cyan arrows, n = 15) or null mutant (*cirl* $^{-/-}$ in black, orange arrows, n = 13) for *cirl*. Myo-II enrichment at the boundary of Toll-8-overexpressing cells is similar in both cases.

(B) MARCM clones in the wing disc. Myo-II is enriched at boundaries (magenta and pink arrows) of clones overexpressing Toll-8 and null mutant for *cirl* (*toll-8* $^{++}$, *cirl* $^{-/-}$ in green) juxtaposed to cells heterozygous (*cirl*$^{+/-}$ in blue, n = 14) or wild type (*cirl*$^{+/+}$ in black, n = 9) for *cirl*.

(C) Quantifications of junctional Myo-II enrichment at clone boundaries for the conditions shown in (A) and (B). With the exception of control clones (black boxplot, images not shown, n = 12), colors of the boxplots correspond to the arrows in (A) and (B).

(D) Myo-II is enriched at the boundary (green arrows) of *cirl*$^{-/-}$ null mutant clones (*cirl*$^{-/-}$ in black) juxtaposed to cells heterozygous (*cirl*$^{+/-}$ in light blue, n = 13) or wild type (*cirl*$^{+/+}$ in dark blue, n = 12) for *cirl*.

(E and F) Junctional Myo-II enrichment (E) and boundary smoothness (F) quantified at clone boundaries for the conditions shown in (D). The black plot in (E) is the same as in (C).

that asymmetric Cirl interfaces at *cirl* mutant clonal boundary enrich Myo-II. Hence, we next investigated whether Toll-8 does induce a Cirl asymmetry at its expression boundary.

Toll-8 generates a Cirl interfacial asymmetry at its expression boundary

To test if Toll-8 is able to induce a Cirl asymmetry at its expression boundary, we first assessed the effect of Toll-8-overexpressing clones on Cirl localization with wing discs expressing Cirl-RFP from the endogenous locus. In control cells that do not overexpress Toll-8, Cirl-RFP was localized at adherens junctions (marked by E-cadherin localization) and in the subapical domain (i.e., the domain above adherens junctions where neighboring cells are in direct contact) (Figures 5A–5A′′, black curve). In cells overexpressing Toll-8-YFP, Cirl-RFP surface levels increased both at adherens junctions and in the subapical

CellPress
OPEN ACCESS

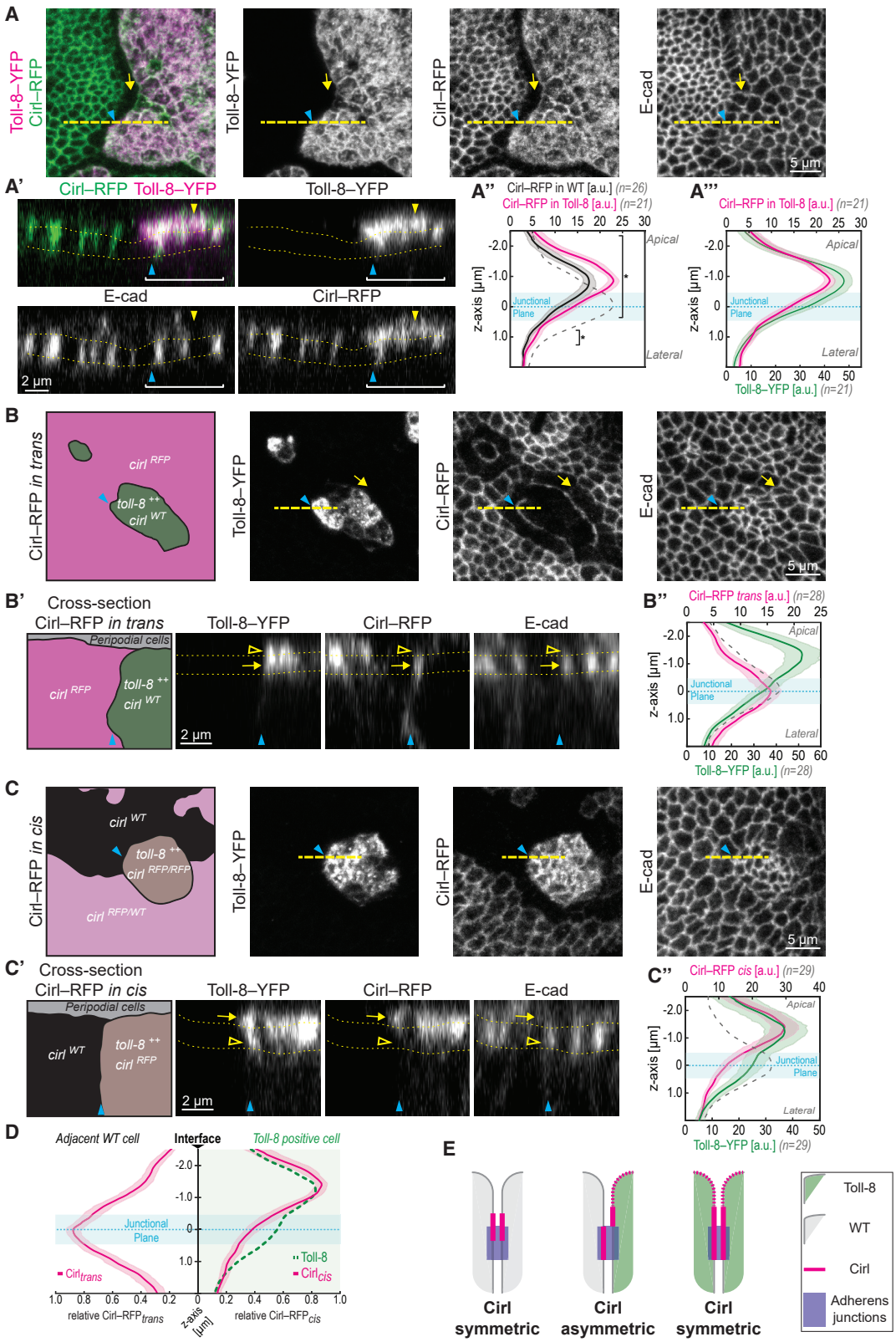

Figure 5. Toll-8 generates Cirl interfacial asymmetry at the boundary of its expression domain

(A) Toll-8-YFP overexpressing clone in a Cirl-RFP wing disc. Toll-8-YFP and anti-Cirl-RFP signals colocalize inside the clone. Cirl is depleted from junctions orthogonal to the clone boundary (yellow arrow). (A′) Optical cross-section of the dashed line in (A) (apical to the top). Dotted lines mark the junctional plane based

(legend continued on next page)

domain (Figures 5A–5A″, magenta curve shifted compared with black curve). Cirl-RFP distribution follows that of Toll-8-YFP (Figures 5A and 5A′, see overlays, and 5A‴), suggesting that Toll-8 re-localizes and stabilizes Cirl. At high levels of expression, Toll-8-YFP was present at the free apical membrane (i.e., the domain where cells are in contact with the extracellular space), which coincided with ectopic localization of Cirl-RFP in this domain (Figure 5A′, yellow arrowheads). This suggests that Toll-8 and Cirl physically interact in *cis*. Strikingly, we observed that Cirl-RFP was depleted from the orthogonal junctions in wild-type cells in direct contact with the boundary of Toll-8-YFP overexpressing cells (Figure 5A, yellow arrow). Thus, Toll-8 affects Cirl localization in *trans*. We observed similar effects on Cirl localization with Toll-6 clonal overexpression (Figure S5A) but not with Toll-2 (Figure S5B), suggesting that Toll-6 also interacts with Cirl while Toll-2 might interact with another protein.

The depletion of Cirl from orthogonal junctions in contact with Toll-8-overexpressing cells led us to ask if Cirl is polarized at the boundary of Toll-8 overexpressing cells in *trans*. To test this, we used MARCM to observe endogenously tagged Cirl-RFP only adjacent to (i.e., in *trans*) Toll-8-YFP-overexpressing cells. Note that in Cirl-RFP-negative cells, untagged endogenous Cirl is present. When Cirl-RFP was present only in *trans*, Cirl-RFP was indeed localized at the clone boundary (Figure 5B, blue arrowheads) and depleted from the junctions orthogonal to the clone boundary (Figure 5B, yellow arrows). This effect did not require the presence of Cirl inside Toll-8-overexpressing cells (Figure S5C). Thus, Cirl is planar polarized in wild-type cells in direct contact with Toll-8 overexpressing cells, suggesting that Toll-8 and Cirl physically interact in *trans*. Surprisingly, at the clone boundary, Cirl-RFP in *trans* strictly colocalized with E-cadherin at adherens junctions and was absent from the subapical domain (Figure 5B′, arrow, and 5B″). We then examined how Cirl-RFP was localized at clonal boundaries in cells overexpressing Toll-8-YFP using MARCM to observe endogenously tagged Cirl-RFP only inside the clone (i.e., in *cis*). When Cirl-RFP was present only in *cis* (Figure 5C), Cirl-RFP was enriched in the subapical domain and tended to be reduced at adherens junctions (Figures 5C′, arrow, and 5C″). Therefore, at cell-cell interfaces between wild-type and Toll-8-overexpressing cells, where cells are in direct contact, Cirl is specifically localized to adherens junctions in *trans* (Figures 5B′ and 5B″) while it is enriched above adherens junctions in *cis* (Figures 5C′ and 5C″), creating an interfacial asymmetry in Cirl localization (Figure 5D). The apicobasal localization of Cirl at either side of Toll-8 clonal boundaries remained unchanged when Cirl was removed from the opposite side of the clone (Figures S5C′ and S5D″), suggesting that Cirl asymmetric localization at the boundary of Toll-8-overexpressing cells is not due to the competition for Toll-8 binding between Cirl in *cis* and in *trans*.

Toll-8 can thus induce an interfacial asymmetry in Cirl apicobasal localization at Toll-8 expression boundary. Our genetic setup does not allow us to assess Cirl localization only at one side of cell interfaces inside Toll-8 overexpressing clones. Given that inside the clone Toll-8 is symmetrically present both in *cis* and in *trans*, we assume that Cirl should be symmetrically localized at these internal interfaces, resulting in Cirl interfacial asymmetry specifically at the Toll-8 expression boundary, and not at internal interfaces (Figure 5E). Since we showed that asymmetric Cirl interfaces between wild-type and *cirl* mutant cells lead to Myo-II enrichment (Figures 4D and 4E), we propose that the interfacial asymmetry of Cirl induced by Toll-8 might be a signal leading to Myo-II enrichment at Toll-8 expression boundaries.

Quantitative differences in Toll-8 expression lead to mutually dependent Toll-8 and Cirl polarity

To further study the dynamic process of Myo-II planar polarization, we performed *ex vivo* live imaging (Dye et al., 2017) of nascent Toll-8-overexpressing clones in cultured wing discs, using a temperature-sensitive GAL80 (GAL80ts) to precisely time the onset of Toll-8 expression. Myo-II enrichment was already observed when Toll-8-YFP was initially restricted to cell-cell interfaces, prior to its subsequent accumulation in the free apical membrane (Figure S6A). This supports the idea that interfacial Toll-8-YFP, instead of Toll-8 in the free apical membrane, is responsible for the polarization of Myo-II.

Likely due to stochasticity in GAL80ts inactivation/GAL4 derepression (Figure 6A; Videos S2, S3, and S4), the asynchronous onset of Toll-8 expression between cells in a given clone led to the generation of dynamic changes in Toll-8 expression, creating quantitative differences in Toll-8 levels between neighboring cells. We found that Myo-II was not only enriched at the boundary of Toll-8-YFP expressing cells facing Toll-8-YFP-negative cells but also enriched at interfaces between cells with different Toll-8-YFP levels (Figure 6A, 100 min, cyan arrow, and S6B; Videos S2 and S3). In this assay, the kinetics of Myo-II polarization at the boundary of cells expressing different levels of Toll-8 is in the range of 10 min (Figure 6A′, between 40 and 50 min, Myo-II became polarized at a Toll-8 interface) and the amplitude of Myo-II polarity is around 2-fold (Figure S6B), which is commensurate with the dynamics and amplitude of Myo-II polarization in the embryonic ectoderm (Bertet et al., 2004; Blankenship et al., 2006). Moreover, as the levels of Toll-8-YFP further increased, once Toll-8-YFP expression reached the same level between

on E-cadherin signals. Both Toll-8 and Cirl are present at the free apical membrane (yellow arrowhead). (A″ and A‴) Intensity of Toll-8 and Cirl (x axis) along the apicobasal axis (y axis). The junctional plane (blue area) is defined by E-cadherin peak levels (dashed gray curve). Cirl levels increase in Toll-8 overexpressing clones both at the junctional plane and in the subapical domain (A″, square brackets, *p < 0.05.) following Toll-8 distribution (A‴).

(B) Toll-8-YFP overexpressing clones (*toll-8*$^{++}$, *cirl* ^{WT} in green) in a wing disc where Cirl-RFP is present only outside of Toll-8 overexpressing clones (*cirl* ^{RFP} in magenta). Cirl is depleted from interfaces orthogonal to the clone boundary (yellow arrow) and accumulates at the clone boundary. (B′) Optical cross-section (dashed line in B) shows Cirl enrichment at the junctional plane (yellow arrow), quantified in (B″).

(C) Toll-8-YFP overexpressing clone with Cirl-RFP present inside (*toll-8*$^{++}$, *cirl* ^{RFP} in brown) facing cells homozygous for untagged Cirl (*cirl*^{WT} in black) or heterozygous for *cirl* ^{RFP} (*cirl*$^{RFP/WT}$ in light magenta). (C′) Optical cross-section (dashed line in C) shows Cirl enrichment above the junctional plane (yellow arrow), quantified in (C″).

(D) Comparison of Cirl apicobasal localization at both sides of Toll-8 clonal boundaries. Cirl is observed at the junctional plane in *trans* and above the junctional plane in *cis* creating a Cirl interfacial asymmetry at Toll-8 clonal boundaries.

(E) Model representing the interfacial asymmetry in Cirl apicobasal localization at Toll-8 expression boundary.

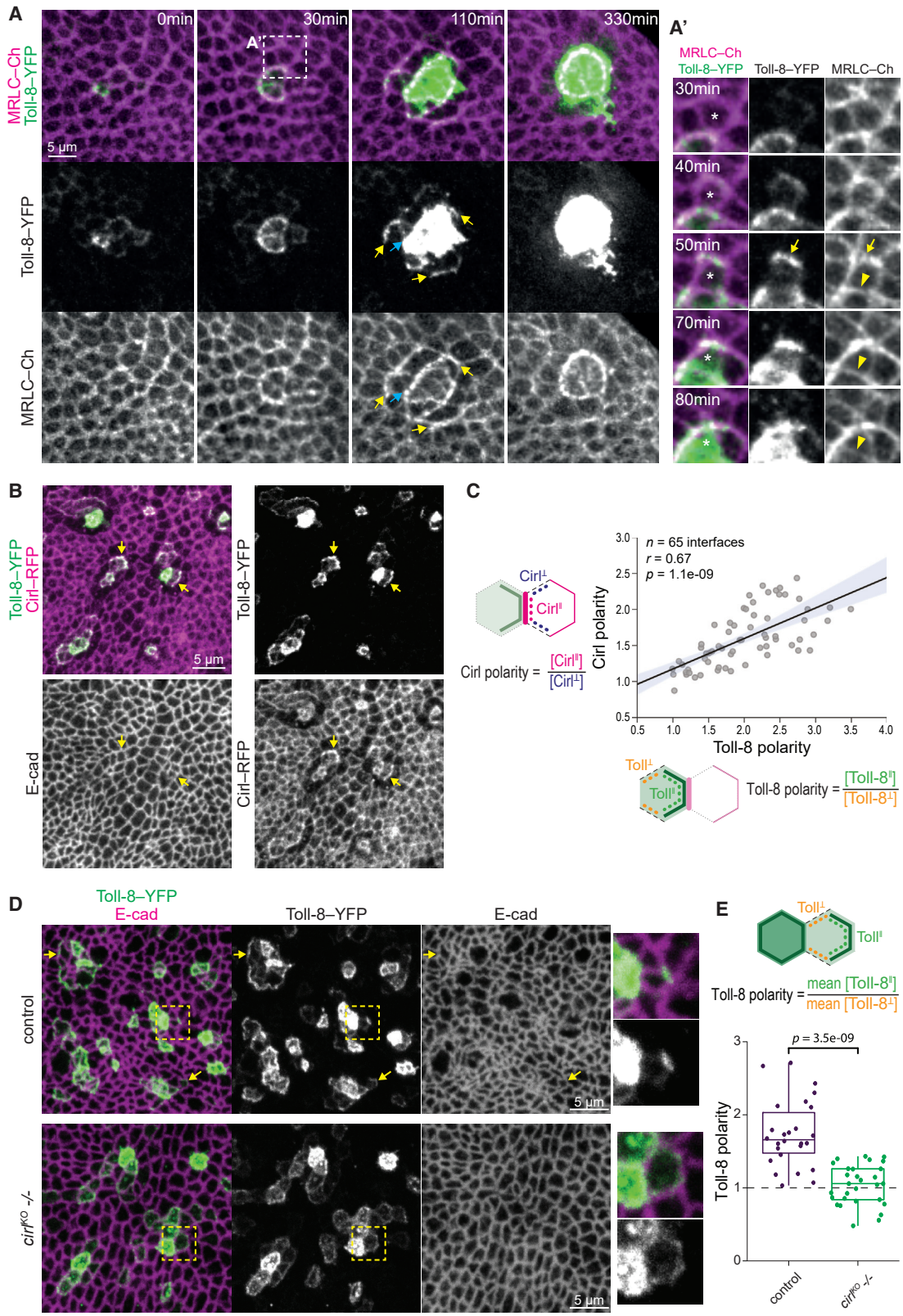

Figure 6. Quantitative differences in Toll-8 expression lead to mutually dependent Toll-8 and Cirl polarity

(A) Stills from a time-lapse movie showing live dynamics of Toll-8-YFP and MRLC-Ch in a nascent Toll-8-YFP-overexpressing clone in a wing disc. Toll-8-YFP becomes detectable at 0 min and increases its levels during the time-lapse. Yellow arrows mark junctions displaying Toll-8 planar polarized enrichment

(legend continued on next page)

these contacting cells, Myo-II enrichment was no longer present at these interfaces (Figure 6A′, arrowheads), and was stabilized only at the boundary of the clone (Figure 6A, 330 min, and S6B). This argues that quantitative differences in Toll-8 expression between neighboring cells polarize Myo-II.

Strikingly, between neighboring cells with quantitative differences in Toll-8 expression levels, Toll-8-YFP was initially planar polarized in cells expressing lower levels and tended to accumulate at interfaces facing away from the cells expressing higher levels (Figures 6A and 6A′, yellow arrows; Videos S2, S3, and S4). Moreover, in cells where Toll-8-YFP was planar polarized, Myo-II was specifically enriched at Toll-8-enriched interfaces, leading to Myo-II planar polarity across several rows of cells (Figure 6A, 110 min, yellow arrows; Videos S2 and S3). Therefore, Toll-8 polarization emerged when neighboring cells express different levels of Toll-8 and this is correlated with polarization of Myo-II.

We then asked how Cirl localization was affected by these nascent polarized patterns of Toll-8. Since live Cirl-RFP signals were too weak, we analyzed anti-Cirl-RFP signals in fixed wing discs. Cirl-RFP was both enriched at interfaces where Toll-8 was planar polarized (Figure 6B, arrows) and reduced in orthogonal interfaces facing cells exhibiting Toll-8 planar polarity. We found a significant correlation between Toll-8 planar polarity and Cirl planar polarity in the neighboring cells in *trans* (Figures 6B and 6C). We conclude that Cirl forms planar polarized patterns in response to Toll-8 polarization. Note that in this experiment, we could not assess Cirl interfacial asymmetry due to the complexity of the genetics required.

Finally, we asked if this transient Toll-8 planar polarity requires Cirl. To test this, we induced nascent Toll-8 overexpression clones in wild-type or *cirl* mutant wing discs. We found that Toll-8 planar polarity was strongly reduced between cells expressing different levels of Toll-8 in the absence of Cirl (Figures 6D and 6E). Thus, the planar polarities of Toll-8 and Cirl mutually depend upon one another. Since Toll-8 and Cirl form a molecular complex, we propose that Toll-8 and Cirl mutually attract each other in a positive feedback, which results in their self-organized polarity at cell interfaces.

DISCUSSION

Our work sheds light on how Myo-II planar polarity emerges from the juxtaposition of cells with distinct genetic identities. We report that Toll-8 asymmetric expression leads to Myo-II polarization independent of other Toll receptors. We identified a cell surface protein complex between Toll-8 and the aGPCR Cirl/latrophilin that is required for Myo-II polarization. Though complete removal of Cirl diminishes Toll-8-induced polarization of Myo-II, removing Cirl from either side of a Toll-8 asymmetric interface does not affect Myo-II polarization. This suggests that Toll-8 expression boundary induces Cirl asymmetry and that this asymmetry itself leads to Myo-II polarization. Consistent with this, Cirl asymmetric expression alone polarizes Myo-II. Moreover, we observed that at the Toll-8 boundary, Cirl is differentially localized in *trans* and in *cis* thus creating a Cirl interfacial asymmetry. This suggests that Cirl asymmetry could be a potential signal for Myo-II enrichment. We have shown that Toll-8/Cirl co-polarity emerges from quantitative differences in Toll-8 expression between neighboring cells via mutual positive feedback. Thus, we propose a conceptual model wherein Toll-8 and Cirl generate self-organized polarity leading to Myo-II enrichment (Figure 7): the first cell expressing Toll-8 (cell A) recruits Cirl in *trans* from neighboring cells by depleting it from their orthogonal interfaces (Figure 7, dashed lines), resulting in Cirl planar polarity in these neighboring cells (Figure 7, panel 1). When one of these cells (cell B) initiates expression of Toll-8, Toll-8 levels are lower than in cell A. Due to this quantitative difference in Toll-8 expression and a preexisting Cirl planar polarity in cell B (where Cirl is depleted from orthogonal interfaces in contact with cell A), Toll-8 in cell B is attracted to the remaining interfaces containing Cirl in *trans*, which are facing away from cell A (Figure 7, panel 2, green arrows and green line in cell B). These new Toll-8-enriched interfaces will stabilize even more Cirl in *trans* at the expense of orthogonal interfaces in the cells adjacent to cell B that do not express Toll-8, thus propagating Cirl planar polarity one row of cells further away (Figure 7, panel 2, magenta arrows). In summary, we propose that quantitative differences in Toll-8 expression between neighboring cells translate into self-organized Toll-8/Cirl/Myo-II planar polarity due to local interactions between Toll-8 and Cirl.

We propose that Toll-8 enriches Myo-II through the asymmetric localization of Cirl in the wing disc. The different localization of Cirl in *cis* and in *trans* of Toll-8 overexpressing cells is not due to *cis* and *trans* Cirl competing for binding with Toll-8. Instead, Toll-8 and Cirl may bind through different protein domains or require different unknown partners in *cis* and in *trans* that are spatially segregated along the apicobasal axis. How asymmetric Cirl enriches Myo-II on both sides of the Toll-8 expression boundary remains to be elucidated. The fact that Myo-II enrichment happens on both sides of the Toll-8 clonal boundaries, even in the absence of Cirl on one side of the boundary, is intriguing. Since Toll-8 is not expressed endogenously in the wing pouch (or expressed at undetectable levels) and given that Toll-8 without its cytoplasmic domain is able to enrich Myo-II, Myo-II polarization on the Toll-8 side is unlikely due to signaling by the Toll-8 cytoplasmic domain. The asymmetry of Cirl extracellular domain may activate other transmembrane

associated with Myo-II enrichment. Cyan arrow indicates an interface between high and low Toll-8 cells. (A′) Zoomed view of a cell (asterisk) that dynamically upregulates expression of Toll-8-YFP during ~50 min. Myo-II is being enriched at junctions that show Toll-8 planar polarity (arrow) and this enrichment is lost once Toll-8 expression reaches similar levels between contacting cells (arrowhead).

(B) Nascent Toll-8-YFP clones in a Cirl-RFP wing disc. Cirl levels are increased at Toll-8-enriched junctions (arrows).

(C) Toll-8 planar polarity versus Cirl planar polarity in *trans* for the condition shown in (B) show a significant positive correlation. Error band indicates the 95% confidence interval.

(D) Toll-8 planar polarity in nascent Toll-8-YFP clones in control (top, n = 26) or *cirl*-null mutant (bottom, n = 29) wing discs. Zoomed views on the right. Toll-8 planar polarity is reduced in the absence of Cirl.

(E) Quantifications of Toll-8 planar polarity in cells with low Toll-8-YFP levels in direct contact with cells with high Toll-8-YFP levels for the conditions shown in (D).

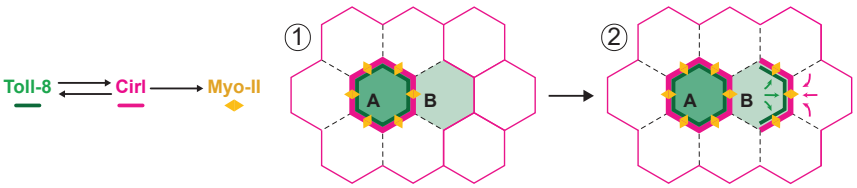

Figure 7. Toll-8 and Cirl form dynamic self-organized patterns

Model proposing mutual attraction between Toll-8 and Cirl leading to the self-organization of Toll-8/Cirl/Myo-II planar polarity. Dashed lines represent interfaces depleted of Cirl.

proteins present on both sides of the clone boundary, in particular other GPCRs, which then signal bidirectionally to enrich Myo-II. Alternatively, Cirl asymmetry may elicit Myo-II polarity by differential recruitment of Rho1 regulators, akin to Cadherin2 in *Ciona* (Hashimoto and Munro, 2019), enriching Myo-II through its intracellular domain on one side of the interface and propagating Myo-II enrichment on the other side through mechanical feedback.

What may prevent symmetric Cirl from signaling to enrich Myo-II? Contrary to the aGPCR Flamingo (Usui et al., 1999), Cirl does not require homophilic *trans* interaction to localize at the membrane (Figure S4D). Interestingly in *C. elegans* latrophilin extracellular domains form stable dimers (Prömel et al., 2012). Hence, extracellular dimerization of Cirl in *trans* could be a mechanism inhibiting symmetric Cirl signaling between neighboring cells. Toll-8 expression boundary could dissociate the Cirl dimers by inducing Cirl asymmetric localization, releasing auto-inhibition and thereby eliciting signaling.

We observed in the wing disc that various quantitative and spatial patterns of Toll-8 have different outputs. Groups of cells expressing homogeneously high levels of Toll-8 form strong Myo-II cables around them similar to those present at tissue compartment boundaries. However, low quantitative differences of Toll-8 expression between neighboring cells can lead to planar polarity of Myo-II across several rows of cells. Thus, mechanical boundaries and planar polarized mechanical interfaces might be considered as a continuum, depending on quantitative inputs of cell surface protein asymmetries, such as Toll-8, interpreted by aGPCRs, such as Cirl. The role of GPCRs and G protein signaling in conveying planar polarized input quantitatively is substantiated by the observation that overexpression of heterotrimeric G protein subunits Gβ/Gγ increases Myo-II planar polarization in early *Drosophila* embryos and converts intercalating cell columns into boundary-like interfaces (Garcia De Las Bayonas et al., 2019).

How do Toll receptors control Cirl activity in the embryo? We were unable to detect Cirl planar polarity in the embryonic ectoderm. Likewise, Toll-8 lacks a detectable planar polarity in this system (Paré et al., 2014). This suggests that in the embryo, Toll-8/Cirl control Myo-II planar polarity without displaying detectable planar polarity. According to evidence in wing discs and our model, the signal for Myo-II polarization is asymmetrical Cirl localization across an interface. One possibility is that in the embryo, though Cirl does not show an axial asymmetry, Cirl could be nonetheless asymmetrically localized along the apicobasal axis between the two sides of vertical interfaces expressing different combinations of Toll receptors (since horizontal interfaces have a similar combination of Toll receptors expressed on each side of the interfaces).

In addition to its instructive role to polarize Myo-II in cooperation with Toll receptors, Cirl may also play a permissive role to activate Myo-II at all junctions in the embryo. Indeed, GPCR signaling is required for both global junctional Rho1/Myo-II activation (independent of planar polarization) (Kerridge et al., 2016), and for their planar polarization *per se* (Garcia De Las Bayonas et al., 2019). The latter requires inputs from Toll receptors, but not the former. Hence, the effect of perturbing GPCR signaling (Cirl mutant) is expected to be more global than just removing the polarity cue (Toll-2,6,8 RNAi). Moreover, Cirl may function in synergy with other GPCRs, such as Smog (Jha et al., 2018; Kerridge et al., 2016).

It was proposed that heterophilic interactions between Toll receptors were required to recruit Myo-II (Paré et al., 2014). Here, we show that asymmetric expression of a single Toll receptor, Toll-8, enriches Myo-II independent of other Toll receptors via its interaction with the aGPCR Cirl. Though we have not looked for biochemical evidence, our results indicate that Toll-6 polarizes Myo-II and Cirl similar to Toll-8 (Figures S2A and S5A). What could be the function of heterophilic interactions between Toll receptors? They could act to reinforce Myo-II planar polarity, as it was proposed in Paré et al. (2014), or alternatively they might reduce Toll receptors-induced Myo-II polarity by competing with Toll-8/Cirl binding. A detailed analysis of Myo-II levels at each interface in the tissue in every single Toll-receptor-null mutant and in each combination of double mutants would be required to answer this question. However, as Toll-2, 6, and 8 all have distinct expression patterns and boundaries in the embryo (Paré et al., 2014), each boundary of expression of a Toll receptor might polarize Myo-II independently of other Toll receptor, as suggested in Tetley et al. (2016). In this case, the multiplicity of Toll receptors expressed in spatially shifted expression patterns would allow polarization of all cells in the ectoderm.

Recently, Toll receptors were shown to be involved in cell competition (Alpar et al., 2018; Meyer et al., 2014) and growth (Germani et al., 2018). Since there is a known interplay between cell competition and mechanics (Levayer et al., 2015, 2016; Moreno et al., 2019; Vishwakarma and Piddini, 2020; Wagstaff et al., 2016), it is tantalizing to suggest a role for Cirl and Toll-8 in this context.

The vertebrate Cirl homolog latrophilins regulate synaptogenesis and repulsive neuronal migration via coincidental *trans*-heterophilic binding with FLRTs and teneurins (Boucard et al., 2014; O'Sullivan et al., 2012; Sando et al., 2019; del Toro et al., 2020). These processes both engage the RhoA pathway in vertebrates (Luo, 2002). Given that this pathway is critical for Myo-II activation in *Drosophila* embryos, it likely mediates Toll-8/Cirl signaling. FLRTs share sequence similarities with Toll-8 (Dolan et al., 2007) and FLRT3 plays an important role in tissue morphogenesis (Karaulanov et al., 2006; Smith and Tickle, 2006; Tomás et al., 2011), which might depend on its interaction with

latrophilins. Moreover, in *Drosophila* the teneurin Ten-m interacts with the LRR protein Tartan to enrich Myo-II at compartment boundaries (Paré et al., 2019), and Cirl might play a role in this system.

The depletion of Cirl around Toll-8 overexpressing cells resembles the effect of Flamingo overexpression on Frizzled localization (Chen et al., 2008; Strutt and Strutt, 2008), both central components of the conserved core PCP pathway (Devenport, 2014). Intriguingly, Flamingo is also an aGPCR and shares sequence homology with Cirl (Langenhan et al., 2013). It is also required for junctional Myo-II activation in the chick neural plate (Nishimura et al., 2012) and during axis extension in Xenopus (Shindo and Wallingford, 2014). The self-organized planar polarization of Toll-8/Cirl identified in our study suggests the possibility that aGPCRs, such as Cirl and Flamingo, are conserved cell surface proteins involved in PCP that evolved different modalities of symmetry breaking. In the core PCP pathway, Flamingo symmetry breaking is thought to be biased by long range mechanical (Aigouy et al., 2010; Aw et al., 2016; Chien et al., 2015) or chemical gradients of adhesion molecules (Fat, Dachsous) or ligands (Wnt) (Aw and Devenport, 2017), which align Flamingo polarity across the tissue. In the Toll-8/Cirl system, Cirl symmetry breaking is potentially triggered by quantitative differences in Toll-8 transcriptional levels between neighboring cells. Directionality of spatial differences in Toll-8 transcriptional levels could define the orientation of Toll-8 and Cirl polarity, resembling the Fat-Ds PCP pathway (Bosveld et al., 2012). Thus, our work illustrates a previously unknown protein complex that generates planar polarized mechanical interfaces instructed by tissue-level cues.

Limitations of the study

One limitation of our study is that it is technically challenging to distinguish Cirl-RFP signals from both sides of an interface in the embryo, since we do not have a way to remove Cirl-RFP signal only from the *cis* or *trans* side as performed via mosaic analysis in the wing disc (which cannot be done in embryos). Analyzing the localization of Cirl with such precision in the embryo will require super-resolution microscopy and the generation of photoactivatable tools.

STAR★METHODS

Detailed methods are provided in the online version of this paper and include the following:

- KEY RESOURCES TABLE
- RESOURCE AVAILABILITY
  - Lead contact
  - Materials availability
  - Data and code availability
- EXPERIMENTAL MODEL AND SUBJECT DETAILS
- METHOD DETAILS
  - Fly strains and genetics
  - Constructs and transgenesis
  - Antibodies
  - Affinity purification mass spectrometry
  - Bright-field live imaging in embryos
  - RNA interference in embryos
  - RT-qPCR experiment
  - Fluorescence live imaging and image processing in embryos
  - Immunofluorescence and image processing in embryos
  - Clonal analysis in wing discs
  - Immunofluorescence and image processing in wing discs
  - *Ex vivo* live imaging and image processing in wing discs
  - Data analysis
- QUANTIFICATION AND STATISTICAL ANALYSIS

SUPPLEMENTAL INFORMATION

Supplemental information can be found online at https://doi.org/10.1016/j.devcel.2021.03.030.

ACKNOWLEDGMENTS

We thank all members of the Lecuit team, B. Aigouy (IBDM, France) for stimulating discussions during the course of this project, the IBDM imaging facility for microscopy assistance, FlyBase for maintaining curated databases and the Bloomington Stock Center for providing fly stocks. We thank T. Langenhan and N. Scholz (Leipzig, Germany) for sharing information about Cirl and fly reagents, and for stimulating discussions. We thank B. Aigouy (IBDM, France) and P. Villoutreix (Centuri, France) for developing the method for quantifying clone smoothness in wing discs. We thank B. Habermann (IBDM, France) for her valuable guidance on performing pairwise alignment between Toll-8 and FLRTs. We are grateful to M. Ludwig (Birmingham, UK), P.F. Lenne (IBDM, France), E. Wieschaus (Princeton, USA), A. Martin (MIT, USA), R. Karess (IJM, France), G. Jiménez (IBMB, Spain) and T. Gregor (Pasteur Institute, France) for the gift of flies and vectors. This work was supported by grants from the European Research Council, European Union (Biomecamorph no. 323027) and the Ligue Nationale Contre le Cancer, France (Equipe Labellisée, 2018). J.L. was supported by the Fondation Bettencourt Schueller, France and the Collège de France. S.H. was supported by an EMBO Long-Term Fellowship (EMBO ALTF 217-2017) and by a Centuri Postdoctoral Fellowship. The Marseille proteomics (IBiSA) is supported by Institut Paoli-Calmettes (IPC) and Canceropôle PACA. Proteomic analyses were done using the mass spectrometry facility of Marseille proteomics (marseille-proteomique.univ-amu.fr) supported by IBISA (Infrastructures Biologie Santé et Agronomie), Plateforme Technologique Aix-Marseille, the Cancéropôle PACA, the Provence-Alpes-Côte d'Azur Région, the Institut Paoli-Calmettes and the Centre de Recherche en Cancérologie de Marseille. We acknowledge the France-BioImaging infrastructure supported by the French National Research Agency (ANR–10–INBS-04-01, Investments for the future).

AUTHOR CONTRIBUTIONS

J.L., Q.M., and T.L. conceived the project. Q.M., J.L., and S.K. performed experiments in embryos, Q.M. analyzed them. J.L. performed all the experiments and data analysis in fixed wing discs. S.H. performed and analyzed live experiments in wing discs and quantified data in Figures 5 and 6. Q.M. and A.L. prepared the samples for the mass spectrometry, which was done and analyzed by S.A. and L.C. J.-M.P. designed and generated the molecular constructs. J.L., Q.M., and T.L. wrote the manuscript, and all authors made comments.

DECLARATION OF INTERESTS

The authors declare no competing interests.

Received: September 8, 2020
Revised: February 23, 2021
Accepted: March 25, 2021
Published: April 30, 2021

REFERENCES

Aigouy, B., Farhadifar, R., Staple, D.B., Sagner, A., Röper, J.C., Jülicher, F., and Eaton, S. (2010). Cell flow reorients the axis of planar polarity in the wing epithelium of drosophila. Cell *142*, 773–786.

Alpar, L., Bergantiños, C., and Johnston, L.A. (2018). Spatially restricted regulation of Spätzle/toll signaling during cell competition. Dev. Cell *46*, 706–719.e5.

Anthoney, N., Foldi, I., and Hidalgo, A. (2018). Toll and toll-like receptor signalling in development. Development *145*, 1–6.

Aw, W.Y., and Devenport, D. (2017). Planar cell polarity: global inputs establishing cellular asymmetry. Curr. Opin. Cell Biol. *44*, 110–116.

Aw, W.Y., Heck, B.W., Joyce, B., and Devenport, D. (2016). Transient tissue-scale deformation coordinates alignment of planar cell polarity junctions in the mammalian skin. Curr. Biol. *26*, 2090–2100.

Bailles, A., Collinet, C., Philippe, J.M., Lenne, P.F., Munro, E., and Lecuit, T. (2019). Genetic induction and mechanochemical propagation of a morphogenetic wave. Nature *572*, 467–473.

Benton, M.A., Pechmann, M., Frey, N., Stappert, D., Conrads, K.H., Chen, Y.T., Stamataki, E., Pavlopoulos, A., and Roth, S. (2016). Toll genes have an ancestral role in axis elongation. Curr. Biol. *26*, 1609–1615.

Bertet, C., Sulak, L., and Lecuit, T. (2004). Myosin-dependent junction remodelling controls planar cell intercalation and axis elongation. Nature *429*, 667–671.

Bielmeier, C., Alt, S., Weichselberger, V., La Fortezza, M., Harz, H., Jülicher, F., Salbreux, G., and Classen, A.K. (2016). Interface contractility between differently fated cells drives cell elimination and cyst formation. Curr. Biol. *26*, 563–574.

Bischof, J., Maeda, R.K., Hediger, M., Karch, F., and Basler, K. (2007). An optimized transgenesis system for Drosophila using germ-line-specific phiC31 integrases. Proc. Natl. Acad. Sci. USA *104*, 3312–3317.

Blankenship, J.T., Backovic, S.T., Sanny, J.S.S.P., Weitz, O., and Zallen, J.A. (2006). Multicellular rosette formation links planar cell polarity to tissue morphogenesis. Dev. Cell *11*, 459–470.

Bosveld, F., Bonnet, I., Guirao, B., Tlili, S., Wang, Z., Petitalot, A., Marchand, R., Bardet, P.L., Marcq, P., Graner, F., and Bellaïche, Y. (2012). Mechanical control of morphogenesis by fat/dachsous/four-jointed planar cell polarity pathway. Science *336*, 724–727.

Bothma, J.P., Garcia, H.G., Esposito, E., Schlissel, G., Gregor, T., and Levine, M. (2014). Dynamic regulation of eve stripe 2 expression reveals transcriptional bursts in living Drosophila embryos. Proc. Natl. Acad. Sci. USA *111*, 10598–10603.

Boucard, A.A., Maxeiner, S., and Südhof, T.C. (2014). Latrophilins function as heterophilic cell-adhesion molecules by binding to teneurins: regulation by alternative splicing. J. Biol. Chem. *289*, 387–402.

Chan, E.H.Y., Chavadimane Shivakumar, P.C., Clément, R., Laugier, E., and Lenne, P.F. (2017). Patterned cortical tension mediated by N-cadherin controls cell geometric order in the drosophila eye. eLife *6*, 1–27.

Chen, W.S., Antic, D., Matis, M., Logan, C.Y., Povelones, M., Anderson, G.A., Nusse, R., and Axelrod, J.D. (2008). Asymmetric homotypic interactions of the atypical cadherin flamingo mediate intercellular polarity signaling. Cell *133*, 1093–1105.

Chien, Y.H., Keller, R., Kintner, C., and Shook, D.R. (2015). Mechanical strain determines the axis of planar polarity in ciliated epithelia. Curr. Biol. *25*, 2774–2784.

Cox, J., Hein, M.Y., Luber, C.A., Paron, I., Nagaraj, N., and Mann, M. (2014). Accurate proteome-wide label-free quantification by delayed normalization and maximal peptide ratio extraction, termed MaxLFQ. Mol. Cell. Proteomics *13*, 2513–2526.

Cox, J., and Mann, M. (2008). MaxQuant enables high peptide identification rates, individualized p.p.b.-range mass accuracies and proteome-wide protein quantification. Nat. Biotechnol. *26*, 1367–1372.

Dahmann, C., Oates, A.C., and Brand, M. (2011). Boundary formation and maintenance in tissue development. Nat. Rev. Genet. *12*, 43–55.

del Toro, D., Carrasquero-Ordaz, M.A., Chu, A., Ruff, T., Shahin, M., Jackson, V.A., Chavent, M., Berbeira-Santana, M., Seyit-Bremer, G., Brignani, S., et al. (2020). Structural basis of teneurin-latrophilin interaction in repulsive guidance of migrating neurons. Cell *180*, 323–339.e19.

Devenport, D. (2014). The cell biology of planar cell polarity. J. Cell Biol. *207*, 171–179.

Dolan, J., Walshe, K., Alsbury, S., Hokamp, K., O'Keeffe, S., Okafuji, T., Miller, S.F., Tear, G., and Mitchell, K.J. (2007). The extracellular leucine-Rich Repeat superfamily; a comparative survey and analysis of evolutionary relationships and expression patterns. BMC Genomics *8*, 320.

Dye, N.A., Popović, M., Spannl, S., Etournay, R., Kainmüller, D., Ghosh, S., Myers, E.W., Jülicher, F., and Eaton, S. (2017). Cell dynamics underlying oriented growth of the drosophila wing imaginal disc. Development *144*, 4406–4421.

Fagotto, F., Rohani, N., Touret, A.S., and Li, R. (2013). A molecular base for cell sorting at embryonic boundaries: contact inhibition of cadherin adhesion by ephrin/Eph-dependent contractility. Dev. Cell *27*, 72–87.

Garcia De Las Bayonas, A., Philippe, J.M., Lellouch, A.C., and Lecuit, T. (2019). Distinct RhoGEFs activate apical and junctional contractility under control of G proteins during epithelial morphogenesis. Curr. Biol. *29*, 3370–3385.e7.

Germani, F., Hain, D., Sternlicht, D., Moreno, E., and Basler, K. (2018). The toll pathway inhibits tissue growth and regulates cell fitness in an infection-dependent manner. eLife *7*, 1–10.

Harmansa, S., Alborelli, I., Bieli, D., Caussinus, E., and Affolter, M. (2017). A nanobody-based toolset to investigate the role of protein localization and dispersal in Drosophila. eLife *6*, 1–22.

Hashimoto, H., and Munro, E. (2019). Differential expression of a classic cadherin directs tissue-level contractile asymmetry during neural tube closure. Dev. Cell *51*, 158–172.e4.

Huang, J., Zhou, W., Dong, W., Watson, A.M., and Hong, Y. (2009). From the cover: directed, efficient, and versatile modifications of the Drosophila genome by genomic engineering. Proc. Natl. Acad. Sci. USA *106*, 8284–8289.

Irvine, K.D., and Wieschaus, E. (1994). Cell intercalation during Drosophila germband extension and its regulation by pair-rule segmentation genes. Development *120*, 827–841.

Jha, A., van Zanten, T.S., Philippe, J.M., Mayor, S., and Lecuit, T. (2018). Quantitative control of GPCR organization and signaling by endocytosis in epithelial morphogenesis. Curr. Biol. *28*, 1570–1584.e6.

Karaulanov, E.E., Böttcher, R.T., and Niehrs, C. (2006). A role for fibronectin-leucine-rich transmembrane cell-surface proteins in homotypic cell adhesion. EMBO Rep *7*, 283–290.

Kerridge, S., Munjal, A., Philippe, J.M., Jha, A., De Las Bayonas, A.G., Saurin, A.J., and Lecuit, T. (2016). Modular activation of Rho1 by GPCR signalling imparts polarized myosin II activation during morphogenesis. Nat. Cell Biol. *18*, 261–270.

Langenhan, T., Aust, G., and Hamann, J. (2013). Sticky signaling–adhesion class G protein-coupled receptors take the stage. Sci. Signal. *6*, re3.

LeGoff, L., Rouault, H., and Lecuit, T. (2013). A global pattern of mechanical stress polarizes cell divisions and cell shape in the growing *Drosophila* wing disc. Development *140*, 4051–4059.

Levayer, R., Dupont, C., and Moreno, E. (2016). Tissue crowding induces Caspase-dependent competition for space. Curr. Biol. *26*, 670–677.

Levayer, R., Hauert, B., and Moreno, E. (2015). Cell mixing induced by myc is required for competitive tissue invasion and destruction. Nature *524*, 476–480.

Li, J., Xie, Y., Cornelius, S., Jiang, X., Sando, R., Kordon, S.P., Pan, M., Leon, K., Südhof, T.C., Zhao, M., and Araç, D. (2020). Alternative splicing controls teneurin-latrophilin interaction and synapse specificity by a shape-shifting mechanism. Nat. Commun. *11*, 2140.

Lim, B., Samper, N., Lu, H., Rushlow, C., Jiménez, G., and Shvartsman, S.Y. (2013). Kinetics of gene derepression by ERK signaling. Proc. Natl. Acad. Sci. USA *110*, 10330–10335.

Ludwig, M.Z., Manu, Kittler, R., White, K.P., and Kreitman, M. (2011). Consequences of eukaryotic enhancer architecture for gene expression dynamics, development, and fitness. PLOS Genet *7*, e1002364.

Luo, L. (2002). Actin cytoskeleton regulation in neuronal morphogenesis and structural plasticity. Annu. Rev. Cell Dev. Biol. *18*, 601–635.

Martin, A.C., Kaschube, M., and Wieschaus, E.F. (2009). Pulsed contractions of an actin-myosin network drive apical constriction. Nature *457*, 495–499.

Meyer, S.N., Amoyel, M., Bergantiños, C., de la Cova, C., Schertel, C., Basler, K., and Johnston, L.A. (2014). An ancient defense system eliminates unfit cells from developing tissues during cell competition. Science *346*, 1258236.

Milán, M., Weihe, U., Pérez, L., and Cohen, S.M. (2001). The LRR proteins Capricious and Tartan mediate cell interactions during DV boundary formation in the Drosophila wing. Cell *106*, 785–794.

Moreno, E., Valon, L., Levillayer, F., and Levayer, R. (2019). Competition for space induces cell elimination through compaction-driven ERK downregulation. Curr. Biol. *29*, 23–34.e8.

Müller, H.-A.J. (2008). Immunolabeling of embryos. Methods Mol Biol *420*, 207–218.

Nishimura, T., Honda, H., and Takeichi, M. (2012). Planar cell polarity links axes of spatial dynamics in neural-tube closure. Cell *149*, 1084–1097.

O'Sullivan, M.L., de Wit, J., Savas, J.N., Comoletti, D., Otto-Hitt, S., Yates, J.R., and Ghosh, A. (2012). FLRT proteins are endogenous latrophilin ligands and regulate excitatory synapse development. Neuron *73*, 903–910.

Paré, A.C., Naik, P., Shi, J., Mirman, Z., Palmquist, K.H., and Zallen, J.A. (2019). An LRR receptor-teneurin system directs planar polarity at compartment boundaries. Dev. Cell *51*, 208–221.e6.

Paré, A.C., Vichas, A., Fincher, C.T., Mirman, Z., Farrell, D.L., Mainieri, A., and Zallen, J.A. (2014). A positional Toll receptor code directs convergent extension in Drosophila. Nature *515*, 523–527.

Prömel, S., Frickenhaus, M., Hughes, S., Mestek, L., Staunton, D., Woollard, A., Vakonakis, I., Schöneberg, T., Schnabel, R., Russ, A.P., and Langenhan, T. (2012). The GPS motif is a molecular switch for bimodal activities of adhesion class G protein-coupled receptors. Cell Rep *2*, 321–331.

Sando, R., Jiang, X., and Südhof, T.C. (2019). Latrophilin GPCRs direct synapse specificity by coincident binding of FLRTs and teneurins. Science *363*, eaav7969.

Schindelin, J., Arganda-Carreras, I., Frise, E., Kaynig, V., Longair, M., Pietzsch, T., Preibisch, S., Rueden, C., Saalfeld, S., Schmid, B., et al. (2012). Fiji: an open-source platform for biological-image analysis. Nat. Methods *9*, 676–682.

Scholz, N., Gehring, J., Guan, C., Ljaschenko, D., Fischer, R., Lakshmanan, V., Kittel, R.J., and Langenhan, T. (2015). The adhesion GPCR latrophilin/CIRL shapes mechanosensation. Cell Rep *11*, 866–874.

Scholz, N., Guan, C., Nieberler, M., Grotemeyer, A., Maiellaro, I., Gao, S., Beck, S., Pawlak, M., Sauer, M., Asan, E., et al. (2017). Mechano-dependent signaling by latrophilin/CIRL quenches cAMP in proprioceptive neurons. eLife *6*, e28360.

Schöneberg, T., and Prömel, S. (2019). Latrophilins and teneurins in invertebrates: no love for each other? Front. Neurosci. *13*, 1–11.

Shevchenko, A., Wilm, M., Vorm, O., and Mann, M. (1996). Mass spectrometric sequencing of proteins from silver-stained polyacrylamide gels. Anal. Chem. *68*, 850–858.

Shindo, A., and Wallingford, J.B. (2014). PCP and septins compartmentalize cortical actomyosin to direct collective cell movement. Science *343*, 649–652.

Smith, T.G., and Tickle, C. (2006). The expression of Flrt3 during chick limb development. Int. J. Dev. Biol. *50*, 701–704.

Stathopoulos, A., and Levine, M. (2005). Localized repressors delineate the neurogenic ectoderm in the early Drosophila embryo. Dev. Biol. *280*, 482–493.

Strutt, H., and Strutt, D. (2008). Differential stability of flamingo protein complexes underlies the establishment of planar polarity. Curr. Biol. *18*, 1555–1564.

Tetley, R.J., Blanchard, G.B., Fletcher, A.G., Adams, R.J., and Sanson, B. (2016). Unipolar distributions of junctional myosin II identify cell stripe boundaries that drive cell intercalation throughout Drosophila axis extension. eLife *5*, 956–963.

Tomás, A.R., Certal, A.C., and Rodríguez-León, J. (2011). FLRT3 as a key player on chick limb development. Dev. Biol. *355*, 324–333.

Usui, T., Shima, Y., Shimada, Y., Hirano, S., Burgess, R.W., Schwarz, T.L., Takeichi, M., and Uemura, T. (1999). Flamingo, a seven-pass transmembrane cadherin, regulates planar cell polarity under the control of Frizzled. Cell *98*, 585–595.

Vishwakarma, M., and Piddini, E. (2020). Outcompeting cancer. Nat. Rev. Cancer *20*, 187–198.

Vizcaíno, J.A., Deutsch, E.W., Wang, R., Csordas, A., Reisinger, F., Ríos, D., Dianes, J.A., Sun, Z., Farrah, T., Bandeira, N., et al. (2014). ProteomeXchange provides globally coordinated proteomics data submission and dissemination. Nat. Biotechnol. *32*, 223–226.

Wagstaff, L., Goschorska, M., Kozyrska, K., Duclos, G., Kucinski, I., Chessel, A., Hampton-O'Neil, L., Bradshaw, C.R., Allen, G.E., Rawlins, E.L., et al. (2016). Mechanical cell competition kills cells via induction of lethal p53 levels. Nat. Commun. *7*, 11373.

Yagi, Y., Nishida, Y., and Ip, Y.T. (2010). Functional analysis of Toll-related genes in Drosophila. Dev. Growth Differ. *52*, 771–783.

Zallen, J.A., and Wieschaus, E. (2004). Patterned gene expression directs bipolar planar polarity in Drosophila. Dev. Cell *6*, 343–355.

STAR★METHODS

KEY RESOURCES TABLE

REAGENT or RESOURCE	SOURCE	IDENTIFIER
Antibodies		
Rat Monoclonal anti-E-Cad	DHSB	RRID: AB_528120
Mouse Monoclonal anti-β-catenin	DHSB	RRID: AB_528089
Mouse Monoclonal anti-LacZ	DHSB	RRID: AB_2314509
Rat Monoclonal anti-HA	Roche	RRID: AB_390918
Rabbit Polyclonal anti-GFP	Thermo Fisher Scientific	RRID: AB_221569
Rabbit Polyclonal anti-GFP	Abcam	RRID: AB_305564
Rabbit Polyclonal anti-RFP	Rockland	RRID: AB_2209751
Donkey anti-Rabbit Alexa Fluor 488 IgG	Thermo Fisher Scientific	RRID: AB_2535792
Donkey anti-Rabbit Alexa Fluor 568 IgG	Thermo Fisher Scientific	RRID: AB_2534017
Donkey anti-Mouse Alexa Fluor 568 IgG	Thermo Fisher Scientific	RRID: AB_2534013
Donkey anti-Mouse Alexa Fluor 647 IgG	Jackson ImmunoResearch Labs	RRID: AB_2340863
Donkey anti-Rat Alexa Fluor 647 IgG	Jackson ImmunoResearch Labs	RRID: AB_2340694
Critical commercial assays		
Direct-zol RNA MiniPrep	Zymo Research	Cat #R2050
iScript™ Reverse Transcription Supermix	Bio-rad	Cat #1708841
TaqMan Fast Advanced Master Mix	Thermo Fisher Scientific	Cat #4444557
RiboMAX™ Large Scale RNA Production System	Promega	Cat #P1300
GFP-Trap® Agarose	ChromoTek	Cat #gta-20; RRID: AB_2631357
Deposited data		
Proteomics Identifications (PRIDE)	EMBL-EBI	RRID: SCR_003411
Experimental models: Organisms/strains		
D.melanogaster: ind-Toll-8FL::HA	This paper	N/A
D.melanogaster: ind-Toll-8ΔLRR::HA	This paper	N/A
D.melanogaster: UASp-Toll-8FL::eGFP	This paper	N/A
D.melanogaster: UASp-Toll-8ΔLRR::eGFP	This paper	N/A
D.melanogaster: UASp-Toll-8ΔCyto::eGFP	This paper	N/A
D.melanogaster: UASt-Toll-8::sYFP2	This paper	N/A
D.melanogaster: UASp-Toll-6FL::eGFP	This paper	N/A
D.melanogaster: UASp-Toll-6ΔLRR::eGFP	This paper	N/A
D.melanogaster: UASp-Toll-6ΔCyto::eGFP	This paper	N/A
D.melanogaster: UASt-Toll-6::sYFP2	This paper	N/A
D.melanogaster: UASp-Toll-2FL::eGFP	This paper	N/A
D.melanogaster: UASp-Toll-2ΔLRR::eGFP	This paper	N/A
D.melanogaster: UASp-Toll-2ΔCyto::eGFP	This paper	N/A
D.melanogaster: UASt-Toll-2::sYFP2	This paper	N/A
D.melanogaster: Toll-8::sYFP2^{BAC}	Paré et al., 2014	N/A
D.melanogaster: Cirl^{KO}[w-]/CyO	Scholz et al., 2015	N/A
D.melanogaster: Cirl^{KO}[w+]/CyO	Scholz et al., 2015	N/A
D.melanogaster: endo-Cirl::RFP	Scholz et al., 2017	N/A
D.melanogaster: sqh-Lifeact::mCherry	Gift from P.F. Lenne	N/A
D.melanogaster: endo-E-cad::eGFP	Bloomington Drosophila Stock Center	BL_60584
D.melanogaster: eve::sYFP2^{BAC}	Ludwig et al., 2011	Flybase: FBal0279504
D.melanogaster: Act5C>STOP>GAL4	Bloomington Drosophila Stock Center	BL_4780

(*Continued on next page*)

Continued

REAGENT or RESOURCE	SOURCE	IDENTIFIER
D.melanogaster: FRT42D	Bloomington Drosophila Stock Center	BL_1802
D.melanogaster: FRT42D arm-LacZ	Bloomington Drosophila Stock Center	BL_7372
D.melanogaster: FRT42D tub-GAL80	Bloomington Drosophila Stock Center	BL_9917
D.melanogaster: tub-GAL80ts	Bloomington Drosophila Stock Center	BL_7108 and BL_7017
D.melanogaster: P{mata4-GAL-VP16}67	Gift from E. Wieschaus	Flybase: FBti0016178
D.melanogaster: sqh-Sqh::mCherry	This paper	N/A
D.melanogaster: sqh-Sqh::mCherry	Gift from A. Martin	N/A
D.melanogaster: sqh-Sqh::eGFP	Gift from R Karess	N/A
Oligonucleotides		
Primers for dsRNA against Toll-2: T7 5'-Tag plus Left: 5'-AGTTTGAATCGAAAC GCGAGGC-3' Right: 5'-TGGAAGA TGTGGCTGGCAT-3'	This paper	N/A
Primers for dsRNA against Toll-6: T7 5'-Tag plus Left: 5'-TCGAAAATCAGC CAACGTGC-3' Right: 5'-CGATTCACG GTTTAGCTGCG-3'	This paper	N/A
Primers for dsRNA against Toll-7: T7 5'-Tag plus Left: 5'-TGGCAACCGTCTG GTTACTC-3' Right: 5'- CACGCA GAGCATCATGAACG-3'	This paper	N/A
Primers for dsRNA against Toll-8: T7 5'-Tag plus Left: 5'-CGTTTGTCGT TCAGCGGATG-3' Right: 5'-ATCGGGGAGGTTATGAGGGG-3'	This paper	N/A
Recombinant DNA		
Plasmid DNA ind-Toll-8FL::HA	This paper	N/A
Plasmid DNA ind-Toll-8ΔLRR::HA	This paper	N/A
Plasmid DNA UASp-Toll-8FL::eGFP	This paper	N/A
Plasmid DNA UASp-Toll-8ΔLRR::eGFP	This paper	N/A
Plasmid DNA UASp-Toll-8ΔCyto::eGFP	This paper	N/A
Plasmid DNA UASp-Toll-6FL::eGFP	This paper	N/A
Plasmid DNA UASp-Toll-6ΔLRR::eGFP	This paper	N/A
Plasmid DNA UASp-Toll-6ΔCyto::eGFP	This paper	N/A
Plasmid DNA UASp-Toll-2FL::eGFP	This paper	N/A
Plasmid DNA UASp-Toll-2ΔLRR::eGFP	This paper	N/A
Plasmid DNA UASp-Toll-2ΔCyto::eGFP	This paper	N/A
Plasmid DNA UASt-Toll-8::sYFP2	This paper	N/A
Plasmid DNA UASt-Toll-6::sYFP2	This paper	N/A
Plasmid DNA UASt-Toll-2::sYFP2	This paper	N/A
Software and algorithms		
Fiji	Schindelin et al., 2012	RRID: SCR_002285
Tissue Analyzer	Aigouy et al., 2010	https://grr.gred-clermont.fr/labmirouse/software/WebPA/
R Project for Statistical Computing	The R Foundation	RRID: SCR_001905
Python Programming Language	Python Software Foundation	RRID:SCR_008394

RESOURCE AVAILABILITY

Lead contact

Further information and requests for resources and reagents should be directed to and will be fulfilled by the Lead Contact, Thomas Lecuit (thomas.lecuit@univ-amu.fr).

Materials availability

Plasmids, FASTA sequences and transgenic fly lines generated in this study are all available on request.

Data and code availability

The mass spectrometry proteomics data have been deposited to the ProteomeXchange Consortium via the PRIDE partner repository with the dataset identifier PRIDE: PXD017895. Codes used in this study are available upon request.

EXPERIMENTAL MODEL AND SUBJECT DETAILS

The experiments were performed on *Drosophila melanogaster* embryos and larvae. The adult flies were maintained under the standard lab conditions in plastic vials at 18°C or 25°C with yeast food. Embryo collection was done in fly cages with agar plates made with apple juice, supplemented with yeast paste. Larvae were grown in plastic vials at 18°C or 25°C and collected at the third instar larvae wandering stage. Please refer to the Key resources table for the details of the fly lines being used.

METHOD DETAILS

Fly strains and genetics

All fly constructs are listed in the Key resources table. The following mutant alleles and insertions were used: *ind-Toll-8^{FL}::HA* (attP40 on 2L), *ind-Toll-8$^{\Delta LRR}$::HA* (attP40 on 2L), *UASp-Toll-8^{FL}::eGFP* (attP40 on 2L), *UASp-Toll-8$^{\Delta LRR}$::eGFP* (attP40 on 2L), *UASp-Toll-8$^{\Delta Cyto}$::eGFP* (attP40 on 2L), *UASt-Toll-8::sYFP2* (VK27 (attP9744) on 3R), *UASp-Toll-6^{FL}::eGFP* (attP40 on 2L), *UASp-Toll-6$^{\Delta LRR}$::eGFP* (attP40 on 2L), *UASp-Toll-6$^{\Delta Cyto}$::eGFP* (attP40 on 2L), *UASt-Toll-6::sYFP2* (VK27 on 3R), *UASp-Toll-2^{FL}::eGFP* (attP40 on 2L), *UASp-Toll-2$^{\Delta LRR}$::eGFP* (attP40 on 2L), *UASp-Toll-2$^{\Delta Cyto}$::eGFP* (attP40 on 2L), *UASt-Toll-2::sYFP2* (attP40 on 2L), *Toll-8::sYFP2^{BAC}* (gift from J. Zallen) (Paré et al., 2014), *Cirl$^{KO[w+]}$*, *Cirl$^{KO[w-]}$* (gifts from T. Langenhan) (Scholz et al., 2015), *Cirl::RFP* knock-in (Scholz et al., 2017) (*Cirl::RFP^{KIN}*, gift from T. Langenhan), *sqh-Lifeact::mCherry* (VK27 on 3R, gift from P.F. Lenne), *E-cad::eGFP* knock-in (Huang et al., 2009) (*E-cad::eGFP^{KIN}*), *eve::sYFP2^{BAC}* (BAC construct, S2E.MSE.eve.YFP, FBal0279504, gift from M. Ludwig) (Ludwig et al., 2011), *hs-FLP* (Chan et al., 2017), *Ubx-FLP* (Bloomington BL 42718), *Act5C>STOP>GAL4* (Bloomington BL 4780), *FRT42D* (Bloomington BL 1802), *FRT42D arm-LacZ* (Bloomington BL 7372), *FRT42D tub-GAL80* (Bloomington BL 9917), *tub-GAL80ts* (Bloomington BL 7108) and *tub-GAL80ts* (Bloomington BL 7017). *67-Gal4* ({matαtub-GAL4-VP16}67) is a ubiquitous, maternally supplied GAL4 driver (gift from E. Wieschaus). MRLC is encoded by the gene *spaghetti squash* (*sqh*, Genebank ID: AY122159). Sqh was visualized using *sqh-Sqh::mCherry* (VK18 (attP9736) on 2R or VK27 (attP9744) on 3R for experiments in the wing disc or a construct on chromosome 2 from A. Martin (Martin et al., 2009) for live-imaging experiments in the embryo) and *sqh-Sqh::eGFP* transgenics (gift from R. Karess).

A list of all the experimental genotypes is given in Table S2.

Constructs and transgenesis

Expression vectors drivers

UASp expression vector driver was generated by inserting a PhiC31 attB sequence downstream from the K10 3'-UTR of pUASp. UASt expression vector driver corresponds to pUASTattB which contains a PhiC31 attB sequence inserted downstream from the SV40 3'-UTR (Bischof et al., 2007).

ind is an early horizontal stripe expression vector driver generated by modifying the *pbphi-evePr-MS2-yellow* (Bothma et al., 2014) (gift from T. Gregor) as follows. First, EVEstr2 enhancer sequence was replaced by the ind$^{1.4}$ enhancer (Lim et al., 2013) (gift from Gerardo Jiménez). Second, a part of Hsp70Bb 5'-UTR was added after the eve basal promoter. Third, MS2-yellow sequence was replaced by a small polylinker for further cloning.

Expression vectors constructs and transgenics

Toll-8 (*Tollo*, CG6890), *Toll-6* (CG7250) and *Toll-2* (18 wheeler, CG8896) whole ORFs were amplified using specific pACMAN genomic plasmids and cloned inside each expression vectors. UASp driven Tolls ORFs were all tagged Cterminally by mEGFP with a GSAG-SAAGSGEF flexible aa linker in between.*UASp-Toll-8^{FL}::eGFP* is the full length Toll-8 (1346aa). *UASp-Toll-8$^{\Delta Cyto}$::eGFP* is a cytoplasmic truncated version of this vector (deletion from aa H1052 to M1346 last aa). In *UASp-Toll-8$^{\Delta LRR}$::eGFP*, all LRR repeats were removed (deletion from aa E99 to L917). *UASp-Toll-6^{FL}::eGFP* is the full length Toll-6 (1514aa). *UASp-Toll-6$^{\Delta Cyto}$::eGFP* is a cytoplasmic truncated version of this vector (deletion from aa H1088 to A1514 last aa). In *UASp-Toll-6$^{\Delta LRR}$::eGFP*, all LRR repeats were removed (deletion from aa A139 to G964). *UASp-Toll-2^{FL}::eGFP* is the full length Toll-2 (1385aa). *UASp-Toll-2$^{\Delta Cyto}$::eGFP* is a cytoplasmic truncated version of this vector (deletion from aa F1026 to V1385 last aa). In *UASp-Toll-2$^{\Delta LRR}$::eGFP*, all LRR repeats were removed (deletion from aa F110 to L900). *UASt-Toll-2::sYFP2, UASt-Toll-6::sYFP2* and *UASt-Toll-8::sYFP2* are Cter sYFP2 tag construct of full length Toll-2,6 and 8 ORFs cloned into UASt using the same GSAGSAAGSGEF flexible aa linker in between. *ind-Toll-8^{FL}::HA* is a Cter HA tag construct of full length Toll-8 with no linker in between. In *ind-Toll-8$^{\Delta LRR}$::HA*, all LRR repeats were removed (deletion from aa E99 to L917).

All recombinant expression vectors were built using "In-Fusion cloning" (Takara Bio), verified by sequencing (Genewiz) and sent to BestGene Incorporate for PhiC31 site specific mediated transgenesis into attP40 (2L, 25C7) or VK27 (attP9744, 3R, 89E11).

Antibodies

All antibodies that are used in this study are listed in the Key resources table. The following primary antibodies were used: rat-anti-E-Cad (1:200, DHSB DCAD2 concentrate), mouse-anti-β-catenin (1:400, DHSB N2 7A1 Armadillo concentrate), mouse-anti-LacZ (1:100, DHSB 40-1a concentrate), rat-anti-HA (1:100, Anti-HA High Affinity rat IgG_1, Roche ROAHAHA). Sqh::eGFP was detected with rabbit-anti-GFP (1:500, Life Technologies A11122 or 1:1000 Abcam ab6556). Cirl::RFP was detected with rabbit-anti-RFP (1:1000, Rockland 600-401-379). The following secondary antibodies were used: donkey-anti-rabbit Alexa Fluor 488 IgG (Life Technologies A 21206), donkey-anti-rabbit Alexa Fluor 568 IgG (Life Technologies A10042), donkey anti-mouse Alexa Fluor 568 IgG (Life Technologies A10037), donkey-anti-mouse Alexa Fluor 647 IgG (Jackson ImmunoResearch 715 605 151) and donkey-anti-rat Alexa Fluor 647 IgG (Jackson ImmunoResearch 712 605 153). All secondary antibodies were used at 1:500.

Affinity purification mass spectrometry

Protein purification and mass spectrometry

Roughly 600 embryos for each sample were collected from overnight cages kept at 25°C for the following crosses: *yw* (control) or females *; 67-GAL4/+; UASt-Toll-8::sYFP2/+*; x males *; 67-GAL4/+; UASt-Toll-8::sYFP2/+*; (Toll-8::YFP maternal and zygotic overexpression), dechorionated with bleach, transferred directly to lysate buffer (10 mM Tris/Cl pH 7.5; 150 mM NaCl; 0.5 mM EDTA; 0.5% NP-40, supplemented with protease and phosphatase inhibitors) and crushed manually on ice over 30 minutes. Lysates were centrifuged to clear debris and protein concentrations of post-centrifugation supernatants were determined. The crude protein yield per lysate sample is usually 1000∼3000 μg. In each experiment, lysates of comparable protein concentration were incubated with pre-rinsed GFP nano-trap agarose resin (Chromotek, gta-20) at 4°C for 90 min, rinsed 3 x and resuspended in 2x Laemmli buffer with DTT. Protein extraction and purification was performed 3 times each for each cross and verified with silver staining. Protein samples were further purified on NuPAGE 4-12% Bis-Tris acrylamide gels (Life Technologies) and treated with in-gel trypsin digestion (Shevchenko et al., 1996) with minor modifications. Peptides were harvested with two extractions, first in 5% formic acid and then in 5% formic acid in 60% acetonitrile. Samples were reconstituted with 0.1% trifluoroacetic acid in 4% acetonitrile and analyzed by liquid chromatography (LC)-tandem mass spectrometry (MS/MS) with an Orbitrap Fusion Lumos Tribrid Mass Spectrometer (Thermo Electron, Bremen, Germany) online with an Ultimate 3000RSLCnano chromatography system (Thermo Fisher Scientific, Sunnyvale, CA). A detailed mass spectrometry protocol is available upon request.

Protein identification and quantification

Relative intensity-based label-free quantification (LFQ) was processed using the MaxLFQ algorithm (Cox et al., 2014) from the freely available MaxQuant computational proteomics platform (Cox and Mann, 2008). Spectra were searched against a *Drosophila melanogaster* database (UniProt Proteome reference, date 2017.08; 21982 entries). The false discovery rate (FDR) at the peptide and protein levels were set to 1% and determined by searching a reverse database. For protein grouping, all proteins that could not be distinguished based on their identified peptides were assembled into a single entry according to the MaxQuant rules. The statistical analysis was done with Perseus program (version 1.5.1.6) from the MaxQuant environment (www.maxquant.org). Quantifiable proteins were defined as those detected in at least 67% of samples in at least one condition. Protein LFQ normalized intensities were base 2 logarithmized to obtain a normal distribution. Missing values were replaced using data imputation by randomly selecting from a normal distribution centered on the lower edge of the intensity values that simulates signals of low abundant proteins using default parameters (a downshift of 1.8 standard deviation and a width of 0.3 of the original distribution). To determine whether a given detected protein was specifically differential, a two-sample t-test was done using permutation-based false discovery rate (pFDR) with a threshold at 0.1% (5000 permutations). The *p*-value was adjusted using a scaling factor s0=1 (Table S1). In Figure 3, differential proteins are highlighted by a cut-off for $\log_2|\text{Fold change}|>2$ and a p-value<0.01. The mass spectrometry proteomics data have been deposited to the ProteomeXchange Consortium via the PRIDE (Vizcaíno et al., 2014) partner repository with the dataset identifier PXD017895.

Bright-field live imaging in embryos

Images of wild-type or mutant embryos were collected on an inverted microscope (Zeiss, AxioVision software) equipped with a programmable motorized stage to record different positions over time (Mark&Find module from Zeiss). Images were acquired every 2 min for 60 minutes from post dorsal movement of the posterior midgut primordium (0 min). The extent of elongation was measured by dividing the travel distance of the posterior midgut primordium at 40 min and normalized to the maximum travel distance.

RNA interference in embryos

dsRNA probes

dsRNA probes were made using PCR product containing the sequence of the T7 promoter (TAATACGACTCACTATAGGG) followed by 18-21 nucleotides specific to the gene. The dsRNA probe against Toll-2 (18w, CG8896) is 393-bp long and located in the 5'UTR region (Forward primer: AGTTTGAATCGAAACGCGAGGC; Reverse primer: ATGCCAGCCACATCTTCCA). The dsRNA probe against Toll-6 (CG7250) is 518-bp long and located in the 5'UTR region (Forward primer: TCGAAAATCAGCCAACGTGC; Reverse primer: CGATTCACGGTTTAGCTGCG). The dsRNA probe against Toll-7 (CG8595) is 749-bp long and located in the coding region (Forward primer: TGGCAACCGTCTGGTTACTC; Reverse primer: CGTTCATGATGCTCTGCGTG). The dsRNA probe against Toll-8 (Tollo, CG6890) is 423-bp long and located in the 5'UTR region (Forward primer: CGTTTGTCGTTCAGCGGATG; Reverse primer: CCCCTCATAACCTCCCCGAT) and does not target the *ind-Toll-8::HA* transgenes. Gel purified PCR products were subsequently

used as a template for the *in vitro* RNA synthesis with T7 polymerase using Ribomax (Promega, P1300). The dsRNA probes were purified using Sure-Clean (Bioline, BIO-37047). Triple dsRNA probes against Toll-2,6,8 and Toll-2,6,7 were prepared and injected at a final concentration of 5 μM each in RNAse-free water.

Embryo injections

Embryos were collected from fresh agar plates in cages kept at 25°C allowed for 30-min egg laying. Embryos were then dechorionated in 50% bleach, rinsed and aligned on cover slips (#1.5) covered with heptane-glue. After a few minutes of desiccation, embryos were covered with Halocarbon 200 oil and injected with dsRNA or RNase-free water. Post-injection embryos were stored at 25°C until live imaging.

RT-qPCR experiment

Toll-2 and Toll-6 knock-down efficiency was estimated by measuring endogenous mRNA level using RT-qPCR by comparing embryos injected or not with triple dsRNA MIX T268. Total RNA extraction from 5 different samples of ~100 gastrulating yw embryos each injected or not was performed using the Direct-zol RNA miniprep kit (Zymo Research, R2050) plus a on-column DNAse I treatment to remove genomic DNA contamination as recommended. Reverse transcription was performed with the iScript kit (Biorad, 1708841) according to the manufacturer's protocol. Real-time PCR was done on a CFX96 QPCR detection system (Bio-RAD) using TaqMan Fast Advanced Master Mix with the following TaqMan probes (Applied Biosystems, Life Technologies), following classical TaqMan probes protocol:

Toll-2=18W= Dm01841837_s1 (position 5228 / GenBank NM_057466, amplicon = 152bp)
Toll-6= Dm01822826_s1 (position 5259 / GenBank NM_001259836, amplicon = 109bp)
RPl32: House-keeping gene reference: Dm02151827_g1: (exon 2-3 boundary, 377 / GenBank NM_001144655, amplicon = 72bp)
RPII140: House-keeping gene: Dm02134593_g1 (exon 2-3 boundary, 2347 / GenBank NM_001300394, amplicon = 78bp)
Act42A: House-keeping gene: Dm02362162_g1 (one exon, 1439 / GenBank NM_078901, amplicon = 108bp)

RT-qPCR conditions were as follows: 50° for 2min; 95° for 10min; 40 cycles [95°C for 15 s and 60°C for 1min]. Analyses were performed in duplicate using five independent injected embryos and controls samples. Beforehand, the three housekeeping genes (Rpl32, RPIII40 and Act42A) were compared to verify absence of any variation between samples (not shown). Transcript levels were first normalized to the chosen housekeeping gene RPl32; and then to the control group. ΔΔCq method was used to estimate relative amounts using the Bio-RAD CFX Maestro software. Further statistical analyses were performed by unpaired t-tests by using the qbasePLUS software version 2 (Biogazelle).

Fluorescence live imaging and image processing in embryos

Live embryos analyzed ranged from Stage 7 to early Stage 8 according to egg laying time (3h~3h30 post egg laying at 25°C) and further morphological criteria (posterior mid-gut primordium displacement <1/4 of egg length). Embryos were aligned on cover slips (#1.5) with heptane-glue and were covered with Halocarbon 200 oil. Dual channel time-lapse imaging was performed on a Nikon Eclipse Ti inverted spinning disc microscope (Roper) with a 100x/1.4 oil-immersion objective at 22°C, controlled by the Metamorph software. Z stacks (step size: 0.5 μm) of 6~10 slices were acquired every 30 seconds, for 15~45 minutes starting from stage 6. Laser power was measured and kept constant across all experiments.

To generate 2D projections in experiments with E-Cad::GFP (Figures 1F and S1A), a custom FIJI macro (Bailles et al., 2019) integrating the 'stack focuser' plugin from M. Umorin was used to perform maximum intensity projection for all channels with 3 Z planes around the junctional plane (labeled by E-cad::GFP). For Figure 3C, a single plane at the junction level is manually selected based on maximum junctional sqh::GFP signals. The resulting 2D images were subjected to a background subtraction procedure using the rolling ball tool (radius 50 pixels). The 2D images were segmented on E-cad::GFP or LifeAct::Ch channels semi-automatically with manual corrections in the FIJI plug-in Tissue Analyzer (Aigouy et al., 2010). The resulting segmentation masks were then dilated by 5 pixels on either side of the junction and used as masks for subsequent quantifications. Cell tracking and quantifications of T1 transitions are performed semi-automatically with Tissue Analyzer with manual correction.

Immunofluorescence and image processing in embryos

Embryos were fixed with 8% formaldehyde for 20 min at room temperature. Embryos were processed and stained according to standard procedures (Müller, 2008). Embryos were mounted in Aqua-Polymount (Polysciences). Images were acquired on a Leica SP8 inverted confocal microscope with a 63x/1.4 NA oil-immersion objective (with exception of Figure S3A acquired on a Zeiss LSM780 with a 63x/1.4 NA oil-immersion objective). Z stacks with step size of 0.25-0.4 μm were collected.

2D images were generated by maximum intensity projections followed by the same procedure as for live imaging experiments in embryos (except for 3-pixel dilatation in segmentation masks generated from β-catenin stainings).

Clonal analysis in wing discs

Flies were allowed to lay eggs in vials for ~8h at 25°C and vials were kept at 25°C until heat-shock.

For clonal overexpression of Tolls (Figures 2, 3I, 5A, S2, S4A, S5A, and S5B) 72h AEL (after egg laying) old larvae were heat-shocked at 37° for 10-14 minutes and dissected after 24h.

For GAL80ts experiments (Figures 6 and S6), 72hr AEL larvae were heat-shocked at 37° for 12 minutes, kept at 18° for 48 hours and subsequently incubated at 30°C for 2h15min in order to inactivate GAL80ts and allow expression of Toll-8::YFP.

For MARCM experiments (Mosaic Analysis with a Repressible Cell Marker, Figures 4A, 4B, 5B, 5C, S4B, S4C, S5C, and S5D), 72h AEL larvae were heat-shocked at 37° for 1h, kept at 18° and heat-shocked again 7 hours later at 37° for 1h. Larvae were kept at 18° for 20 hours, shifted to 25° and dissected 24h later. Keeping the larvae at 18° allowed growth of the clones in the presence of no/low levels of Toll-8 expression. Larvae to observe *cirl* mutant clones (Figure 4D) were treated the same way.

Immunofluorescence and image processing in wing discs

Staged larvae were dissected in PBS, transferred to 4% PFA in PBS and fixed under agitation for 18 min at room temperature. After fixation, wing discs were first rinsed with PBS, then extensively washed with PBT (PBS plus 0.2% Triton-X100) and blocked in PBT with 5% normal donkey serum (NDS, Jackson Immuno Research Laboratories, 017-000-001) for at least 30 min at room temperature, followed by incubation with primary antibody in 2% NDS overnight at 4 °C. The next day wing discs were washed in PBT and incubated in secondary antibody with 2% NDS for 1h30min at room temperature. After six rounds of washes with PBT, samples were mounted in Mowiol (Sigma-Aldrich, 324590). Larval mouth hooks were used as spacers in the experiments where Myo-II was observed. Images were acquired on a Leica SP8 inverted confocal microscope with a 63x/1.4 NA oil-immersion objective. Toll-8::YFP and Sqh::Ch were visualized with their endogenous fluorescence. Image stacks with step size of 0.25-0.5 μm were collected.

Peripodial signal was masked from the image stacks in ImageJ to avoid interference with signals from the wing disc proper. 2D projections were generated using the aforementioned custom stack focuser macro in ImageJ, projecting two z planes around the junctional plane of each cell (detected by E-cad staining, except Figures 4A and 4B, projected on Sqh::Ch signals). This allows to project the entire wing pouch independently of the shape of the wing disc. The 2D-projected stacks were then segmented on E-cad stainings (except Figures 4A and 4B segmented on Sqh::Ch signals) using Tissue Analyzer (Aigouy et al., 2010).

Ex vivo live imaging and image processing in wing discs

The culture medium used for long-term time lapse imaging of wing imaginal disc explants is described in Dye et al. (Dye et al., 2017). In short, Grace's insect medium (Sigma G9771, without sodium bicarbonate) was buffered with 5mM BisTris and the pH adjusted to 6.6-6.7. Subsequently the medium was sterile filtered (0.2μm pore size) and kept at 4°C for up to 4 weeks. At the day of the experiment the medium was supplemented with 5% fetal bovine serum (FBS), Penicillin-Streptomycin (final 1x from a 100x stock solution, Sigma P4333) and warmed to 30°C in a water bath. Just before dissection of the larvae, 20-Hydroxyecdysone (20E, Sigma, H5142) was added to yield a total concentration of 20nM. 20E was kept as a 1000x stock solution in ethanol at -20°C. For the experiment, 72h AEL larvae were heat-shocked at 37° for 12 minutes, kept at 18° for 48 hours and subsequently incubated at 30°C for 2h15min in a water bath. Subsequently, larvae were floated out of the food using 30% glycerol and washed in sterile water twice. Surface sterilization in 70% Ethanol was followed by another wash in sterile water and then in medium. Larvae were dissected in culture medium, wing discs isolated and mounted on a round cover slip. In order to restrict disc movement during imaging, discs were covered by a porous membrane (Whatman cyclopore polycarbonate membranes; Sigma, WHA70602513) using two stripes of double-sided tape as spacers. Finally, this sandwich was mounted in an Attofluor cell chamber (A7816, Invitrogen) and filled with 1ml of medium and covered with Parafilm M (P7793, Sigma-Aldrich) to avoid evaporation. Discs were imaged on a Nikon Eclipse Ti inverted spinning disc microscope (Roper) equipped with an incubation chamber heated to 30°C. Imaging was done using a 60x/1.2 NA water-immersion objective (Figures 6A and S6; Videos S2 and S3) or a 100x/1.4 NA oil-immersion objective (Video S4). Dual imaging of Toll-8::YFP and Sqh::Ch was performed by simultaneous excitation of fluorophores with 515nm and 561nm laser lines using a dichroic mirror to image on two cameras (Evolve 512, Photometrics). Stacks of 40 slices with 0.7μm spacing were acquired every 10min (60x movies) or every 5min (100x movies).

A maximum projection of the disc proper junctional plane was obtained by masking the peripodial epithelium and the lateral portion of the disc proper manually in ImageJ based on sqh::Ch signals. Background subtraction was done using a rolling ball (50px radius) in ImageJ.

Data analysis

Definition of expression interfaces

When references channels (Toll-8::HA, Toll-8::YFP, Toll-8::GFP, or LacZ staining) were available, expression interfaces were defined from reference channels in Tissue Analyzer.

To define horizontal cell rows in Figure 1F, cell rows were counted from the ventral midline, with the 4th cell row (most ventral) being 2 rows away from the ventral midline. The boundary between the 2nd and the 3rd cell rows is consistent with the position of *ind* ventral expression boundary.

To define vertical cell columns in Figures S1A and S1B, parasegment boundaries were visualized with Eve::YFP, with the anterior boundary of Eve::YFP signal defined as the parasegment boundary between even- and odd-numbered parasegments. Thus, cell columns 1-4 belong to odd-numbered parasegments (Eve::YFP+), while 5-8 belong to even-numbered parasegments (Eve::YFP-).

Quantification of junctional Myo-II intensities

Raw pixel intensities from segmented junctions were measured in Tissue Analyzer. To extract data tables containing raw pixel intensities from Tissue Analyzer, a customized R procedure was developed using the RSQLite package. Adjusted junctional pixel intensities were obtained by subtracting mean cytoplasmic intensity value measured on each image. Enrichment was calculated as ratios of adjusted junctional intensity values between junctions of interest and those in nearby wild-type tissues (Figures 1A and 2A).

Quantification of boundary smoothness

Boundary smoothness for ventral *ind* expression boundary in the embryo was calculated as the ratio between distance between two end vertices over total junctional length (Figure 1A). Boundary smoothness value approaches 1 as the boundary gets smoother.

For clone smoothness in the wing disc, an original method developed by P. Villoutreix (Centuri, France) was implemented in Tissue Analyzer by B. Aigouy (IBDM, France) under the plugin 'Clone wiggliness'. In brief, the boundary of the clone was extracted, the vertices present at the clone boundary were ordered, and an angle was calculated for each vertex with its two neighboring vertices present at the clone boundary (Figure 2A). A mean value per clone was then calculated and this value is getting closer to 180° if the clone is smooth.

Quantification of apical-basal protein localization (Figure 5)

Protein localization and concentration along the apical-basal axis was quantified as described in Harmansa et al. (Harmansa et al., 2017) from high-z-resolution image stacks (0.35μm slice spacing, acquired on a Leica SP8 confocal microscope using a 63x/1.4 NA oil-immersion objective) of wing discs expressing Toll-8::YFP, Cirl::RFP and stained for the junctional marker E-Cadherin (E-cad). Optical cross-sections were obtained by using the 'reslice' option in Fiji software (ImageJ; National Institute of Health) and subsequently background was subtracted ('rolling ball' radius of 50px). From these cross sections, junctional fluorescence intensity profiles of E-cad, Toll-8::YFP and Cirl::RFP were extracted along a line of 0.6μm width (corresponding to approximately the width of a junction) using the 'plot profile' function in Fiji. Average profiles from different junctions/discs were computed by using the peak of the E-cad profile to align individual profiles. Average profiles were calculated in Excel software (Microsoft) and plotted in Python software using the Seaborn library (line plot function, error bands show the 95% confidence interval computed by bootstrapping). In the plots the junctional plane is visualized by a blue band that is defined as the 0.5μm above and below the average E-cad peak.

Quantification of Toll-8 and Cirl planar polarity (Figures 6B–6E)

We restricted our analysis to single cells expressing low Toll-8::YFP levels in the vicinity of a high Toll-8::YFP expressing cell. This ensured that each junction included in our computation only contained Toll-8::YFP originating from the single cell that was quantified. For each single cell, junctional Toll-8::YFP levels were extracted (using the segmented line tool in ImageJ, line width = 6px) along the parallel junctions (Toll-$8^{\parallel}$, the junctions not being in contact with the high Toll-8 expressing cell) and along the two junctions being in direct contact with high Toll-8 expressing cell (Toll-$8^{\perp}$). Toll-8::YFP enrichment at parallel junctions was computed by calculating the ratio between mean Toll-$8^{\parallel}$ and mean Toll-$8^{\perp}$ levels (Figure 6E, scheme). Cirl planar polarity has been computed in an analogous way (Figure 6C, scheme). To test for a correlation between Cirl and Toll-8 planar polarities, polarity values for each doublet of cell was plotted and linear fitting was performed using Python (Seaborn library for plotting and the Stats library to compute the least square regression and *p*-value).

Data visualization

With the exception of Figures 5, 6C, S5, and S6, data visualization was performed in R with customized scripts. The following custom packages were used: ''fields'' and ''ggplot2''. Plots shown in Figures 5, 6C, S5, and S6 were plotted in Python using the Seaborn library.

QUANTIFICATION AND STATISTICAL ANALYSIS

All measurements were performed in 8-100 independent experiments. Each embryo and clone in the wing disc is considered as an independent experiment. Box-plot elements are defined as follows: center line represents the median; box limits represent the first and third quartiles (the 25th and 75th percentiles); upper whisker extends from the box limit to the largest value no further than 1.5x interquartile range from the box limit and lower whisker extends from the box limit to the smallest value at most 1.5x interquartile range from the box limit; all data points are plotted on the graph. The exact values of n for each graph are reported in the figure legends or in the figure. *p*-values were calculated using the Mann-Whitney U test in R, except from Figure 5A″(two-sided *t*-test with unequal variance) and Figure 6C (two-sided t-test performed using the Python Stats library). In all figures, n.s.: $p > 0.05$. No statistical method was used to predetermine sample size. The experiments were not randomized, and the investigators were not blinded to allocation during experiments and outcome assessment.

Developmental Cell, Volume *56*

Supplemental information

Formation of polarized contractile interfaces by self-organized Toll-8/Cirl GPCR asymmetry

Jules Lavalou, Qiyan Mao, Stefan Harmansa, Stephen Kerridge, Annemarie C. Lellouch, Jean-Marc Philippe, Stephane Audebert, Luc Camoin, and Thomas Lecuit

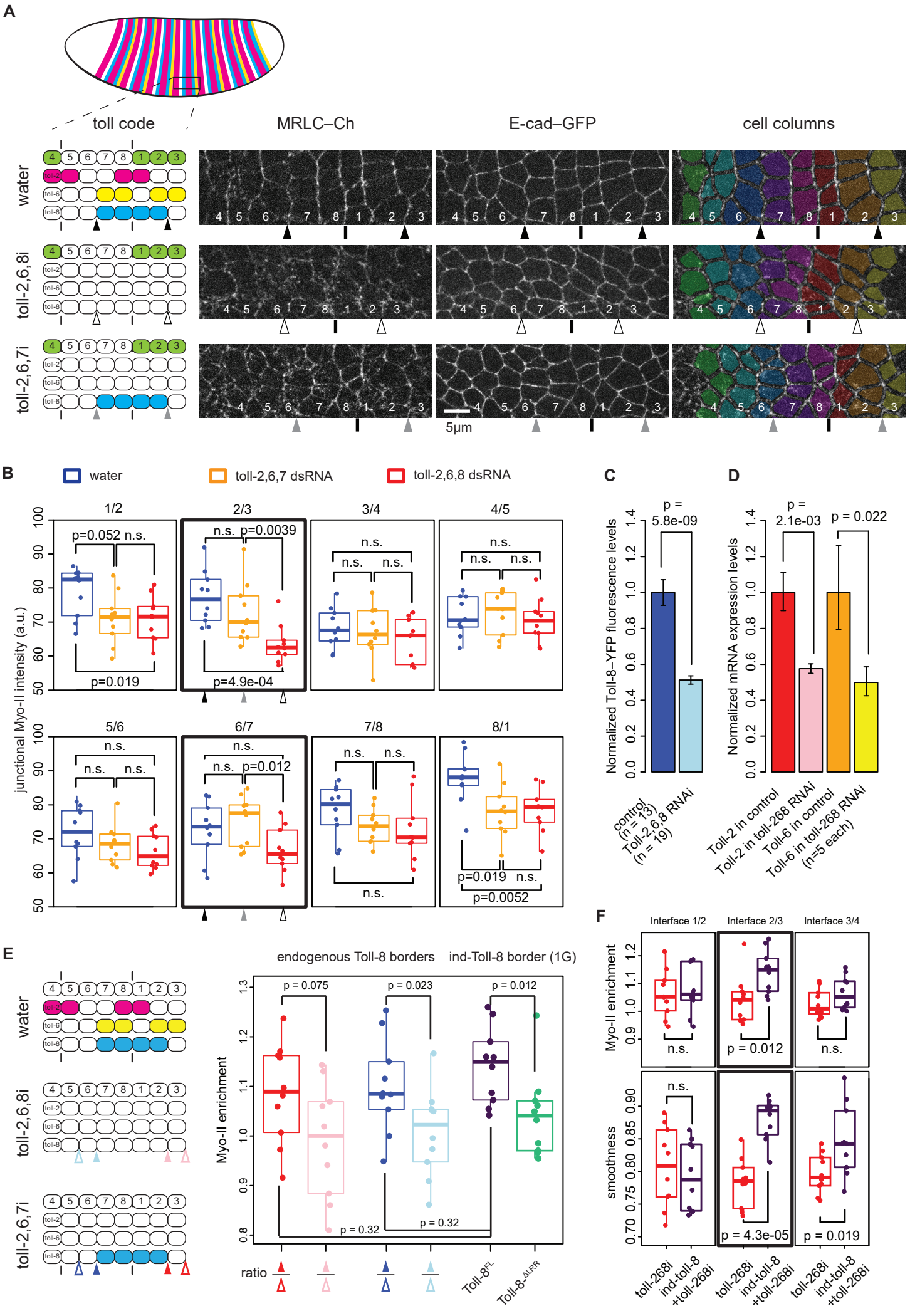
A
toll code
MRLC–Ch
E-cad–GFP
cell columns
water
toll-2,6,8i
toll-2,6,7i
5µm
B
water
toll-2,6,7 dsRNA
toll-2,6,8 dsRNA
junctional Myo-II intensity (a.u.)
1/2
2/3
3/4
4/5
5/6
6/7
7/8
8/1
p=0.052 n.s.
p=0.019
n.s. p=0.0039
p=4.9e-04
n.s.
p=0.012
p=0.019 n.s.
p=0.0052
C
Normalized Toll-8–YFP fluorescence levels
p = 5.8e-09
control (n = 13)
Toll-2,6,8 RNAi (n = 19)
D
Normalized mRNA expression levels
p = 2.1e-03
p = 0.022
Toll-2 in control
Toll-2 in toll-268 RNAi
Toll-6 in control
Toll-6 in toll-268 RNAi
(n=5 each)
E
endogenous Toll-8 borders
ind-Toll-8 border (1G)
Myo-II enrichment
p = 0.075
p = 0.023
p = 0.012
p = 0.32
p = 0.32
ratio
Toll-8FL
Toll-8-ΔLRR
F
Interface 1/2
Interface 2/3
Interface 3/4
Myo-II enrichment
smoothness
n.s.
p = 0.012
p = 4.3e-05
p = 0.019
toll-268i
ind-toll-8 +toll-268i

Figure S1. Endogenous Toll-8 is able to enrich Myo-II at its expression boundaries independent of Toll-2,6 (related to Figure 1).

(A) Schematics of endogenous Toll-2,6,8 expression in embryos under various conditions (top left). Cell columns 1-4: odd parasegments (eve–YFP+, green in the schematics); 5-8: even parasegment (eve–YFP-). Arrowheads show the two boundaries of Toll-8 expression at positions 2/3 and 6/7. See methods for details. Still images from time lapse movies of stage 7 to early stage 8 embryos injected with water (top), dsRNAs against Toll-2,6,8 (middle) and dsRNAs against Toll-2,6,7 (bottom). Note that Toll-7 is not expressed during germband extension. Triple Toll-2,6,7 RNAi was performed to keep the total load of dsRNA comparable to the triple Toll-2,6,8 RNAi condition. Pseudo colors represent cell columns (right). In all panels, vertical bars represent parasegment boundaries where Myo-II is enriched despite of Toll-2,6,8 knockdowns. Arrowheads demark boundaries of the Toll-8 expression domain in embryos injected with water (black), dsRNAs against Toll-2,6,8 (white) or Toll-2,6,7 (grey), where Myo-II is enriched in the sole presence of Toll-8 (bottom).

(B) Quantifications of junctional Myo-II levels at indicated interfaces in embryos injected with water (blue, n=10), dsRNAs against Toll-2,6,7 (orange, n=10) and dsRNAs against Toll-2,6,8 (red, n=10). Black, white and grey arrowheads show quantifications of representative interfaces highlighted in (A).

(C) BAC-Toll-8-YFP (Paré et al., 2014) fluorescence levels in control embryos or in embryos injected with dsRNAs against Toll-2,6,8.

(D) Normalized mRNA expression levels obtained by RT-qPCR for Toll-2 and Toll-6 in control embryos or in embryos injected with dsRNAs against Toll-2,6,8. Toll-2,6,8 RNAi leads to a significant reduction of the expression of all three Toll receptors in the embryo.

(E) Quantification of Myo-II enrichment ratio at the endogenous boundary of the Toll-8 expression domain (interfaces 2/3, n=10; and 6/7, n=10) compared with Myo-II enrichment ratio at the ventral borders of ind-Toll-8 (as reported in Figure 1G). Myo-II enrichment ratios at both endogenous Toll-8 borders are not significantly different from the ind-Toll-8 ventral border. Myo-II is more enriched when Toll-8 is asymmetrically expressed than when Toll-8 is absent from both sides.

(F) Additional quantifications for Figures 1F-H. Quantifications of junctional Myo-II enrichment (top) and boundary smoothness (bottom) at interfaces 1/2 (left, interfaces within the ind-Toll-8^{FL}–HA domain), 2/3 (center, boundary interfaces) and 3/4 (right, interfaces within the wild-type tissue).

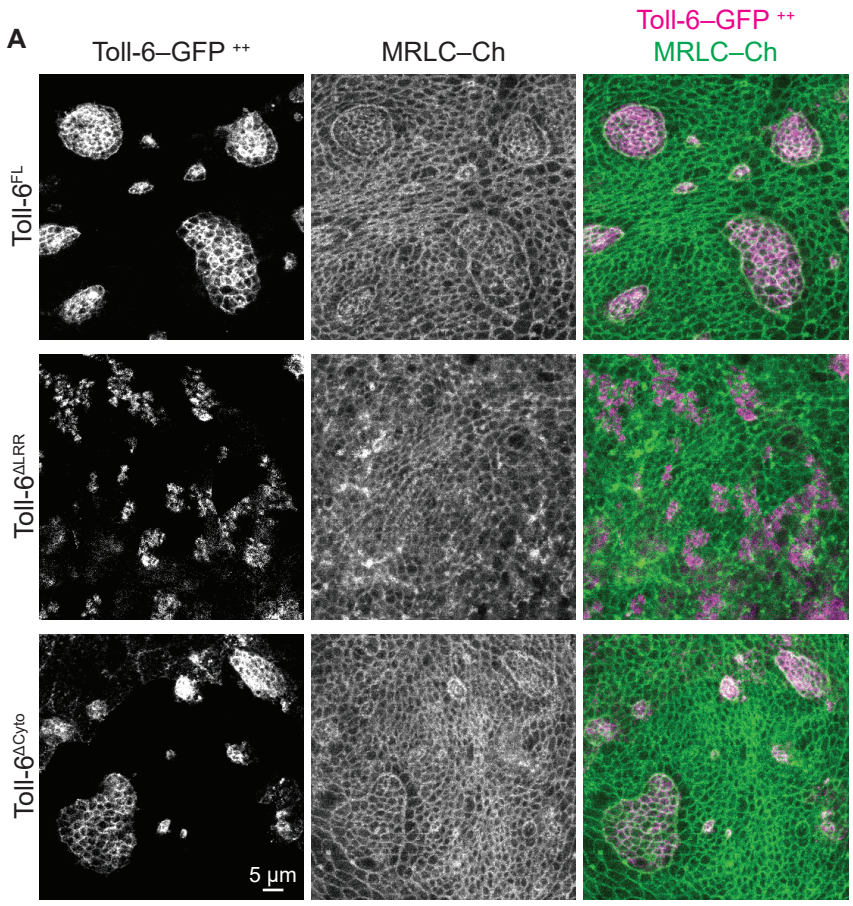
A
Toll-6–GFP ++
MRLC–Ch
Toll-6–GFP ++
MRLC–Ch
Toll-6FL
Toll-6ΔLRR
Toll-6ΔCyto
5 µm

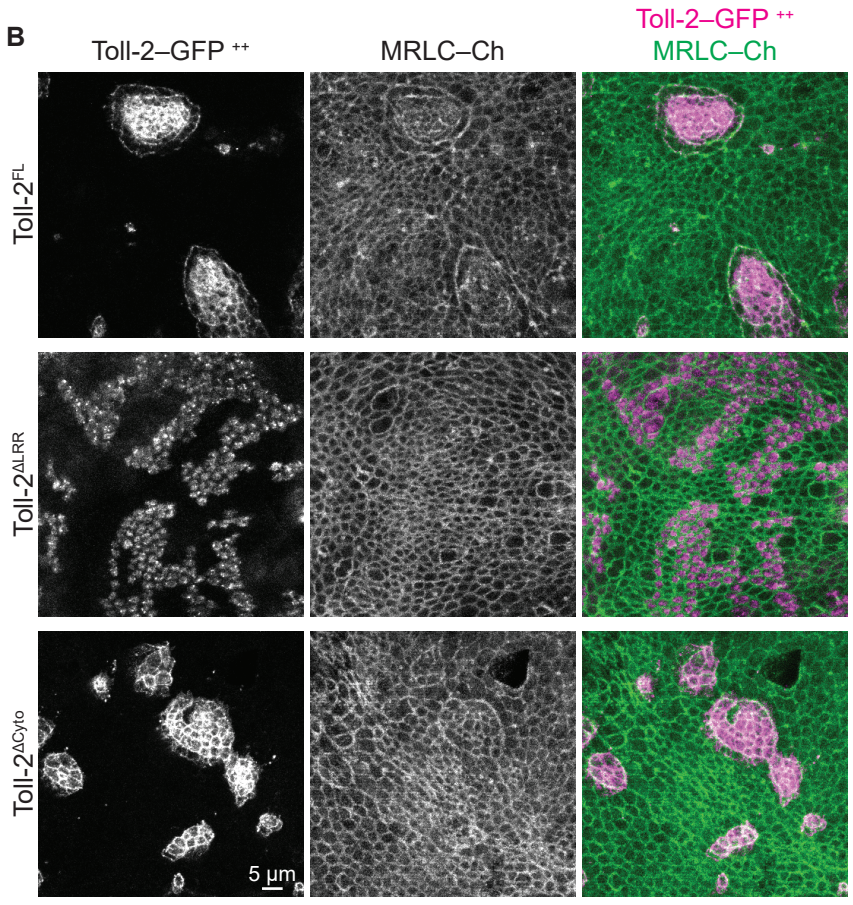
B
Toll-2–GFP ++
MRLC–Ch
Toll-2–GFP ++
MRLC–Ch
Toll-2FL
Toll-2ΔLRR
Toll-2ΔCyto
5 µm

Figure S2. Asymmetric expression of Toll-6 and Toll-2 without their cytoplasmic tails leads to Myo-II enrichment in wing discs (related to Figure 2).

(A) Fixed Toll-6–GFP and MRLC–Ch signals from wing disc clones overexpressing full length Toll-6 (Toll-6^{FL}, top), Toll-6 with the extracellular LRRs removed (Toll-$6^{\Delta LRR}$, middle), or Toll-6 with the intracellular cytoplasmic tail removed (Toll-$6^{\Delta Cyto}$, bottom). Myo-II enrichment requires the extracellular LRRs but not the cytoplasmic tail of Toll-6.

(B) Fixed Toll-2–GFP and MRLC–Ch signals from wing disc clones overexpressing full length Toll-2 (Toll-2^{FL}, top), Toll-2 with the extracellular LRRs removed (Toll-$2^{\Delta LRR}$, middle), or Toll-2 with the intracellular cytoplasmic tail removed (Toll-$2^{\Delta Cyto}$, bottom). Myo-II enrichment requires the extracellular LRRs but not the cytoplasmic tail of Toll-2.

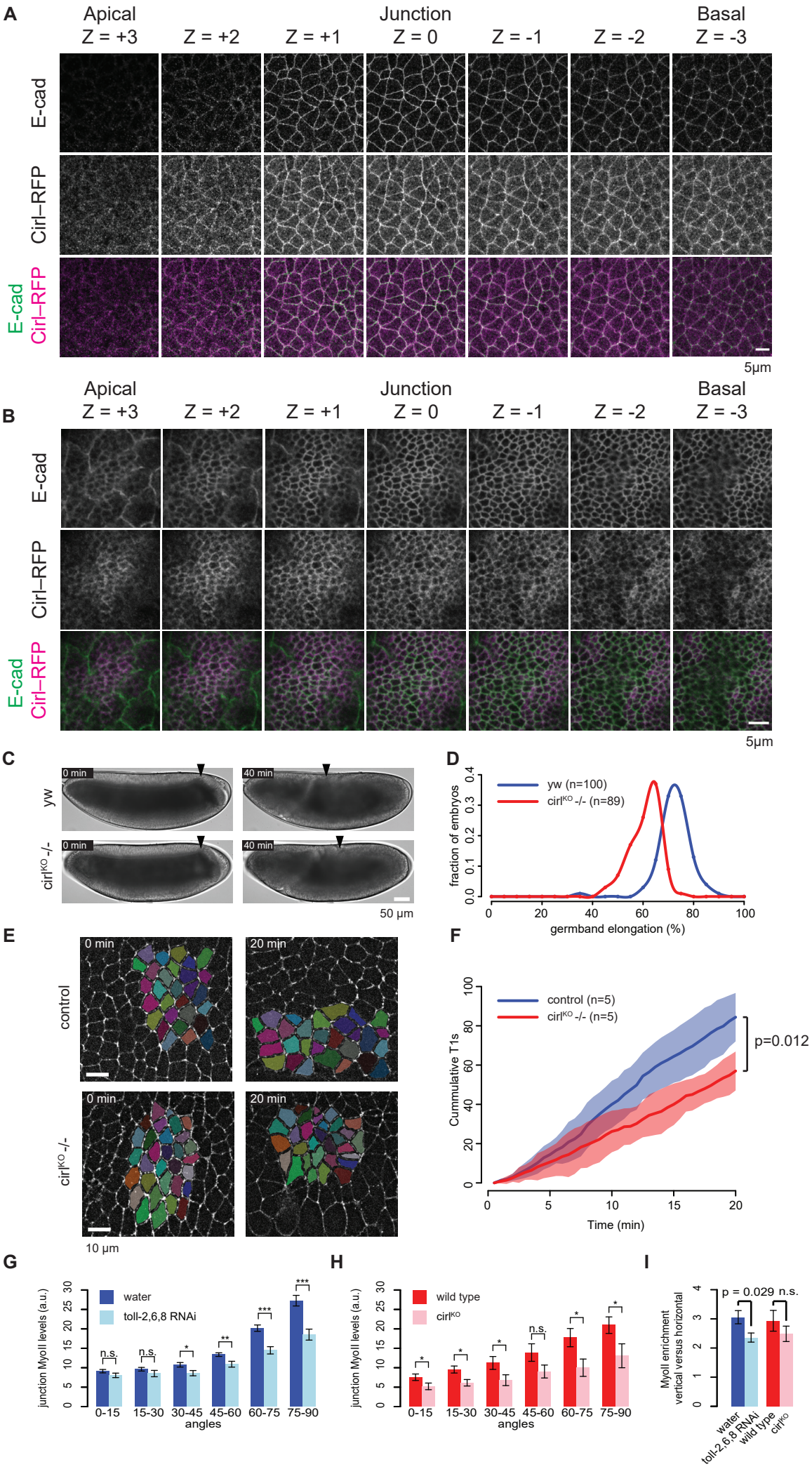
A
Apical
Junction
Basal
Z = +3
Z = +2
Z = +1
Z = 0
Z = -1
Z = -2
Z = -3
E-cad
Cirl–RFP
E-cad
Cirl–RFP
5µm
B
Apical
Junction
Basal
Z = +3
Z = +2
Z = +1
Z = 0
Z = -1
Z = -2
Z = -3
E-cad
Cirl–RFP
E-cad
Cirl–RFP
5µm
C
yw
cirlKO -/-
0 min
40 min
0 min
40 min
50 µm
D
yw (n=100)
cirlKO -/- (n=89)
fraction of embryos
germband elongation (%)
E
control
cirlKO -/-
0 min
20 min
0 min
20 min
10 µm
F
control (n=5)
cirlKO -/- (n=5)
p=0.012
Cummulative T1s
Time (min)
G
water
toll-2,6,8 RNAi
junction MyoII levels (a.u.)
n.s.
n.s.
*
**
***
***
0-15
15-30
30-45
45-60
60-75
75-90
angles
H
wild type
cirlKO
junction MyoII levels (a.u.)
*
*
*
n.s.
*
*
0-15
15-30
30-45
45-60
60-75
75-90
angles
I
Myoll enrichment vertical versus horizontal
p = 0.029 n.s.
water
toll-2,6,8 RNAi
wild type
cirlKO

Figure S3. Localization of Cirl in the *Drosophila* embryonic germband and wing disc cells, and its requirement in embryonic axis extension and cell intercalations (related to Figure 3).

(A) Anti E-cad (green) and anti Cirl–RFP (magenta) signals in the ectoderm epithelium in stage 7 *Drosophila* embryos. Sequential Z planes are shown from apical (left) to basal (right). Step size: 0.38 µm.

(B) Anti E-cad (green) and anti Cirl–RFP (magenta) signals in the wing disc pouch epithelium. Sequential Z planes are shown from apical (left) to basal (right). Step size: 0.25 µm. In both (A) and (B), Cirl–RFP is localized at cell-cell interfaces around adherens junctions.

(C) Axial extension at 0 and 40 minutes in *yw* (top, n=100) and $cirl^{KO}$ -/- (bottom, n=89) embryos. 0 min is defined as the beginning of axial extension. Arrowheads denote the dorsal edge of the posterior midgut primordium. Axial extension is slowed down in the absence of *cirl*.

(D) Histogram of axial extension for *yw* (blue, n=100) and $cirl^{KO}$ -/- (red, n=89) embryos for the conditions shown in (C).

(E) Still images from time lapse movies in *wt* (top, *n*=5) or $cirl^{KO}$ -/- (bottom, *n*=5) embryos. LifeAct–Ch marks cell outlines. Pseudo colors mark tracked cells. 0 min is defined as the beginning of axial extension.

(F) Cumulative numbers of T1 transitions in *wt* (blue, *n*=5) or $cirl^{KO}$ -/- (red, *n*=5) embryos for conditions shown in (E). Solid lines represent mean values, shaded areas represent standard deviation. *p*-value is calculated for total numbers of T1 transitions at the end of 20 minutes between *wt* and $cirl^{KO}$ -/- embryos.

(G and H) Junctional Myo-II levels binned by junction orientations (0-15°: horizontal junctions; 75-90°: vertical junctions) in water (dark blue, *n*=10) and Toll-2,6,8 dsRNA (light blue, *n*=10) injected embryos (G), and in wild type (dark red, *n*=8) and $cirl^{KO}$ (light red, *n*=8) embryos (H). *: $p < 0.05$; **: $p < 0.01$; ***: $p < 0.001$; n.s.: $p > 0.05$.

(I) Myo-II amplitude of polarity calculated as the enrichment ratio of vertical junctions (angles 75-90) over horizontal junctions (angles 0-15) for conditions shown in (G) and (H).

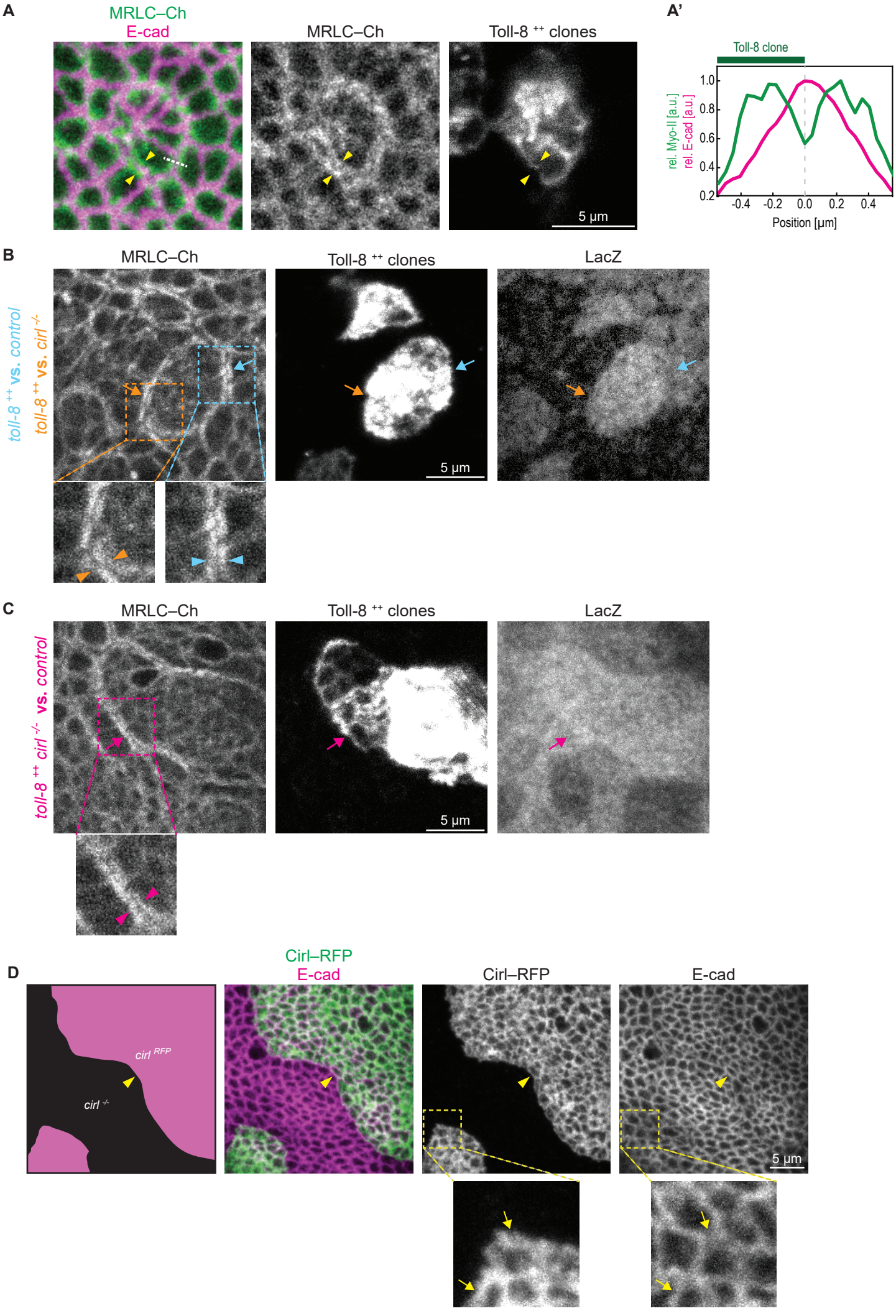
A
MRLC–Ch
E-cad
MRLC–Ch
Toll-8 ++ clones
5 µm
A'
Toll-8 clone
rel. Myo-II [a.u.]
rel. E-cad [a.u.]
1.0
0.8
0.6
0.4
0.2
-0.4
-0.2
0.0
0.2
0.4
Position [µm]
B
MRLC–Ch
Toll-8 ++ clones
LacZ
toll-8 ++ vs. control
toll-8 ++ vs. cirl -/-
5 µm
C
MRLC–Ch
Toll-8 ++ clones
LacZ
toll-8 ++ cirl -/- vs. control
5 µm
D
Cirl–RFP
E-cad
cirl RFP
cirl -/-
Cirl–RFP
E-cad
5 µm

Figure S4. Myo-II is enriched on both sides of the Toll-8 expression boundary (related to Figure 4).

(A) Fixed MRLC–Ch, E-cad and Toll-8–YFP signals from wing disc clones overexpressing Toll-8. Myo-II is enriched on both sides of the boundary of the clone. (A') shows the intensity profile quantified along the dashed white line in (A).

(B) Myo-II signals in MARCM clones in the wing disc where cells overexpressing Toll-8–YFP (*toll-8* $^{++}$, *lacZ* $^{+/+}$, green in Figure 4A) are juxtaposed with control cells heterozygous (*cirl* $^{+/-}$, *lacZ* $^{+/-}$, blue in Figure 4A, cyan arrow) or null mutant (*cirl* $^{-/-}$, *lacZ* $^{-/-}$, black in Figure 4A, orange arrow) for *cirl*. The cyan and orange arrowheads on the zoomed images indicate Myo-II enrichment on both sides of clone boundaries (related to Figure 4A).

(C) MARCM clones in the wing disc. Myo-II is enriched at clone boundaries (magenta arrow) where cells overexpressing Toll-8–YFP and null mutant for *cirl* (*toll-8* $^{++}$, *cirl* $^{-/-}$, *lacZ* $^{+/+}$, green in Figure 4B) are juxtaposed with cells heterozygous (*cirl* $^{+/-}$, *lacZ* $^{+/-}$ in blue in Figure 4B) or *wild-type* (*cirl* $^{+/+}$, *lacZ* $^{-/-}$ in black in Figure 4B) for *cirl*. The magenta arrowheads on the zoomed image mark Myo-II enrichment on both sides of the clone boundary (related to Figure 4B).

(D) Cirl–RFP is still localized in wild-type cell interfaces in contact with *cirl* mutant cells (arrowheads and arrows).

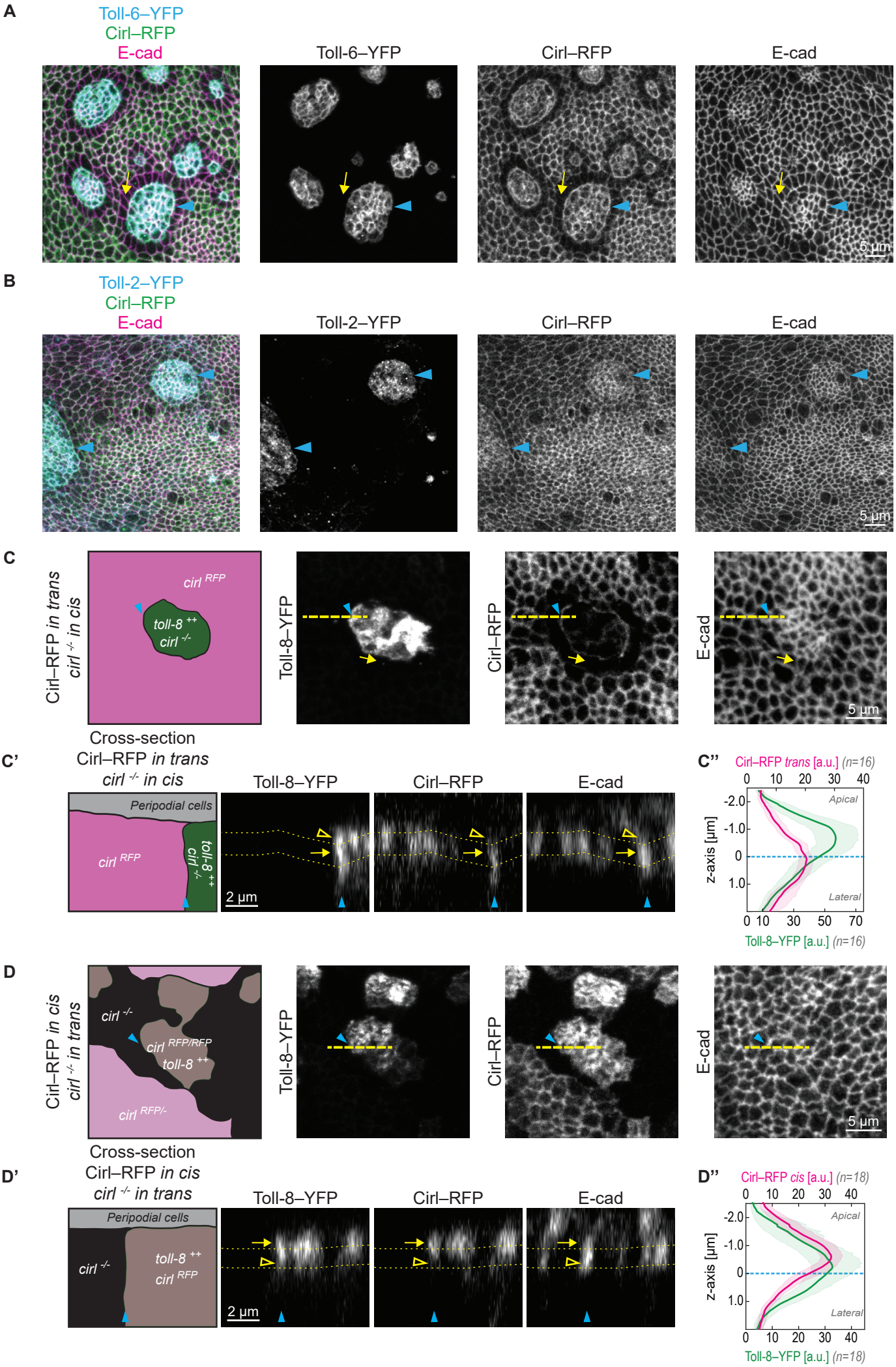
A
Toll-6–YFP
Cirl–RFP
E-cad
Toll-6–YFP
Cirl–RFP
E-cad
5 µm
B
Toll-2–YFP
Cirl–RFP
E-cad
Toll-2–YFP
Cirl–RFP
E-cad
5 µm
C
Cirl–RFP in trans
cirl -/- in cis
cirl RFP
toll-8 ++
cirl -/-
Toll-8–YFP
Cirl–RFP
E-cad
5 µm
Cross-section
Cirl–RFP in trans
cirl -/- in cis
C'
Peripodial cells
cirl RFP
toll-8 ++
cirl -/-
Toll-8–YFP
Cirl–RFP
E-cad
2 µm
C''
Cirl–RFP trans [a.u.] (n=16)
0 10 20 30 40
-2.0
-1.0
0
1.0
z-axis [µm]
Apical
Lateral
0 10 30 50 70
Toll-8–YFP [a.u.] (n=16)
D
Cirl–RFP in cis
cirl -/- in trans
cirl -/-
cirl RFP/RFP
toll-8 ++
cirl RFP/-
Toll-8–YFP
Cirl–RFP
E-cad
5 µm
Cross-section
Cirl–RFP in cis
cirl -/- in trans
D'
Peripodial cells
cirl -/-
toll-8 ++
cirl RFP
Toll-8–YFP
Cirl–RFP
E-cad
2 µm
D''
Cirl–RFP cis [a.u.] (n=18)
0 10 20 30 40
-2.0
-1.0
0
1.0
z-axis [µm]
Apical
Lateral
0 10 20 30 40
Toll-8–YFP [a.u.] (n=18)

Figure S5. Effect of Toll-6 and Toll-2 overexpression on Cirl distribution in the wing disc (related to Figure 5).

Blue arrowheads indicate clone boundaries in all panels.

(A) Toll-6–YFP overexpressing clone in a Cirl–RFP wing disc. Cirl–RFP is depleted from junctions orthogonal to the clone boundary (arrow).

(B) Toll-2–YFP overexpressing clone in a Cirl–RFP wing disc. Cirl–RFP localization is not affected by Toll-2 overexpression.

(C) Same experimental setup as in Figure 5B, with the exception that *cirl* is null mutant instead of untagged in Toll-8 overexpressing clones (*toll-8* $^{++}$, *cirl* $^{-/-}$ in green). Planar polarity of Cirl in wild-type cells neighboring Toll-8 overexpressing clones is not disturbed by the absence of Cirl inside the clones. (C') Optical cross-section (dashed line in (C)) shows Cirl–RFP enrichment at the junctional plane (yellow arrow), quantified in (C'').

(D) Same experimental setup as in Figure 5C, with the exception that *cirl* is null mutant instead of untagged in cells facing Toll-8 overexpressing clones (*cirl* $^{-/-}$ in black). (D') Optical cross-section (dashed line in (D)) shows Cirl–RFP enrichment above the junctional plane (yellow arrow), quantified in (D'').

Error bands indicate the 95% confidence interval in (C'') and (D'').

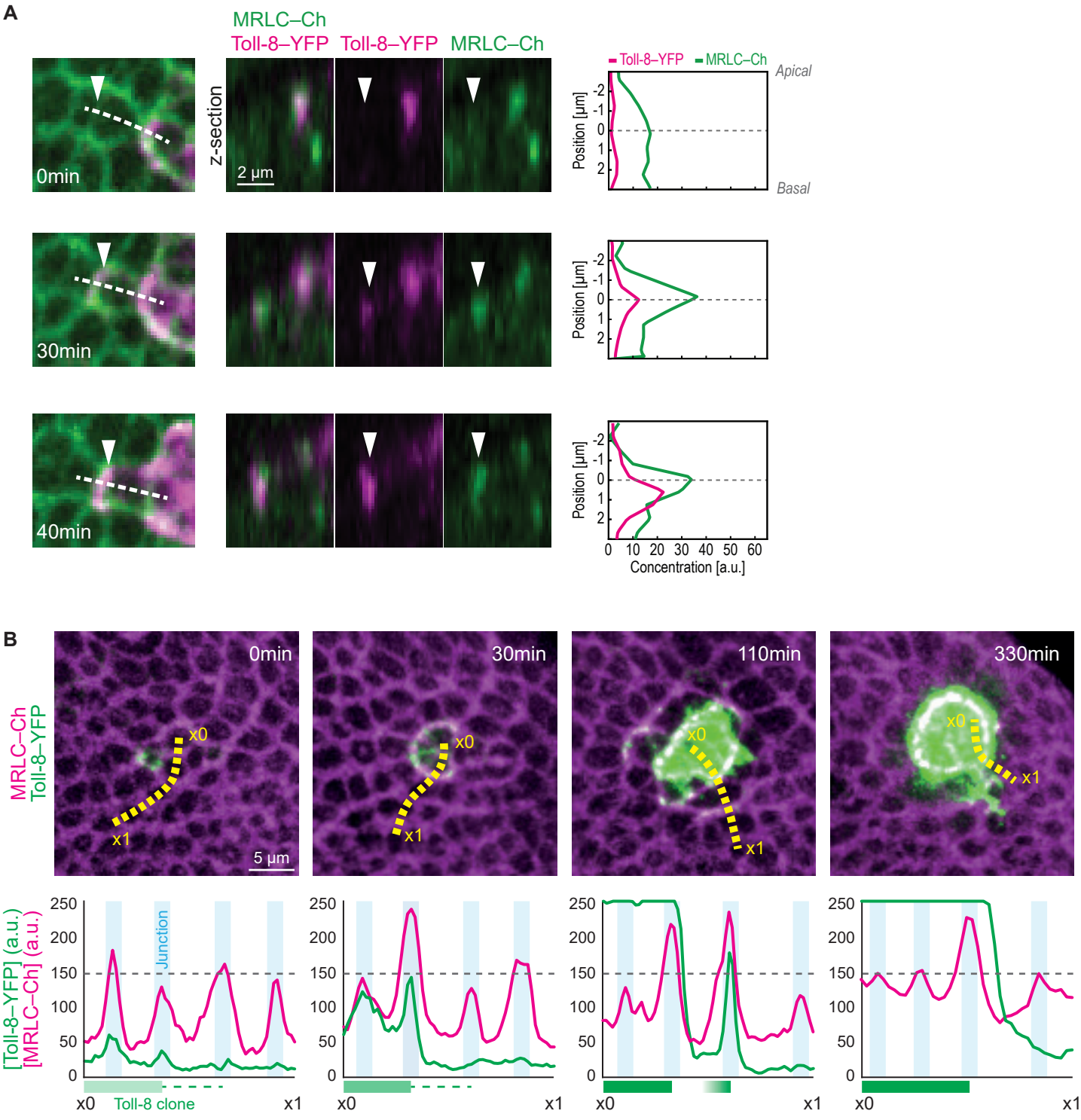
A
MRLC–Ch
Toll-8–YFP Toll-8–YFP MRLC–Ch
z-section
0min
30min
40min
2 µm
Toll-8–YFP MRLC–Ch
Apical
Basal
Position [µm]
-2
-1
0
1
2
0 10 20 30 40 50 60
Concentration [a.u.]
B
MRLC–Ch
Toll-8–YFP
0min
30min
110min
330min
x0
x1
5 µm
[Toll-8–YFP] (a.u.)
[MRLC–Ch] (a.u.)
250
200
150
100
50
0
Junction
Toll-8 clone

Figure S6. Additional quantifications of nascent Toll-8 overexpressing clones in wing disc movies (related to Figure 6).

(A) Stills from a movie showing a nascent Toll-8–YFP overexpressing clone in a wing disc (left) and corresponding optical cross-sections (middle) at positions indicated by the dashed lines in the left panels. Quantifications (right) of Toll-8–YFP and MRLC–Ch levels along the apicobasal axis of a cell interface (arrowhead) at subsequent time-points in a cell starting to express Toll-8–YFP at t=~0min. Myo-II enrichment is observed when Toll-8–YFP is localized exclusively to cell-cell interfaces (t=30min and 40min).

(B) Quantifications of temporal dynamics of Toll-8–YFP (green) and MRLC–Ch (magenta) at the boundary of a nascent Toll-8–YFP overexpressing clone in the wing disc (panels taken from Figure 6A). Toll-8–YFP and MRLC–Ch levels were quantified along a line (yellow, from x0 to x1) at representative stages of clonal Toll-8 upregulation. Myo-II is enriched at the boundary of Toll-8–YFP expressing cells facing Toll-8–YFP negative cells (middle left). Myo-II is also enriched at interfaces between cells expressing different levels of Toll-8–YFP (middle right) leading to multiple rows of Myo-II enrichment. Once Toll-8–YFP levels equalize between cells, Myo-II only remains enriched at junctions that display differences in Toll-8 expression (right).